Article

Cell

Replication Fork Activation Is Enabled by a Single-Stranded DNA Gate in CMG Helicase

Graphical Abstract

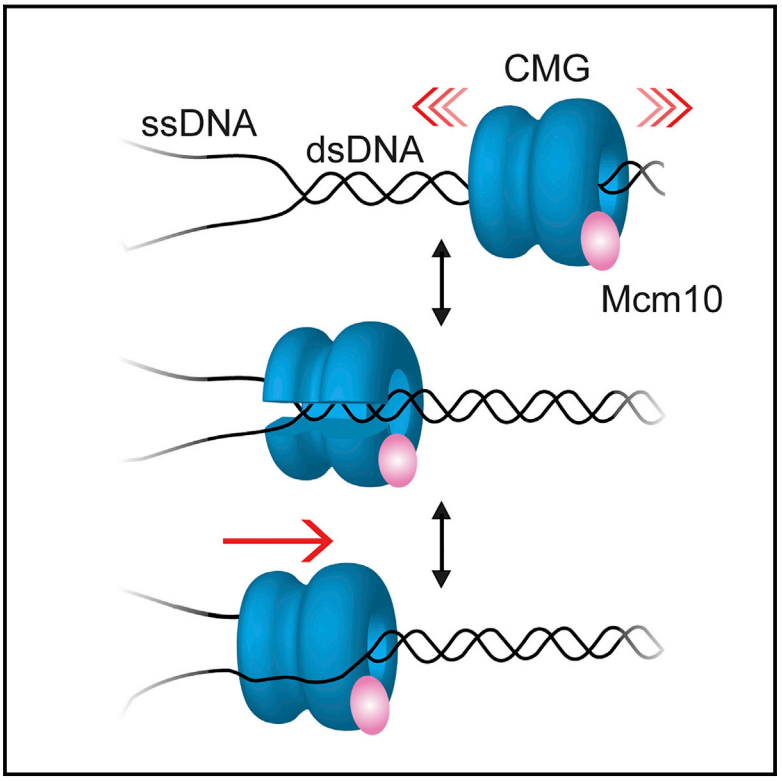

Highlights

- Eukaryotic CMG helicase employs a gate in its ring to switch between ss and dsDNA
- Gating enables CMG to vacate a replication fork when uncoupled from DNA polymerase
- CMG diffuses on dsDNA and uses this gate to enter a fork and restart replication
- Mcm10, an essential replisome factor, tethers CMG to DNA during the gating process

Authors

Michael R. Wasserman, Grant D. Schauer, Michael E. O'Donnell, Shixin Liu

Correspondence

odonnel@rockefeller.edu (M.E.O.), shixinliu@rockefeller.edu (S.L.)

In Brief

A "gate" in the eukaryotic CMG helicase allows it to switch between single- and double-stranded DNA, providing an explanation for how replication forks can continue past DNA lesions and restart after stalling

Wasserman et al., 2019, Cell *178*, 600–611
July 25, 2019
https://doi.org/10.1016/j.cell.2019.06.032

CellPress

Cell

Article

Replication Fork Activation Is Enabled by a Single-Stranded DNA Gate in CMG Helicase

Michael R. Wasserman,[1,4] Grant D. Schauer,[2,4] Michael E. O'Donnell,[2,3,5,*] and Shixin Liu[1,5,6,*]
[1]Laboratory of Nanoscale Biophysics and Biochemistry, The Rockefeller University, New York, NY 10065, USA
[2]Laboratory of DNA Replication, The Rockefeller University, New York, NY 10065, USA
[3]Howard Hughes Medical Institute, The Rockefeller University, New York, NY 10065, USA
[4]These authors contributed equally
[5]These authors contributed equally
[6]Lead Contact
*Correspondence: odonnel@rockefeller.edu (M.E.O.), shixinliu@rockefeller.edu (S.L.)
https://doi.org/10.1016/j.cell.2019.06.032

SUMMARY

The eukaryotic replicative helicase CMG is a closed ring around double-stranded (ds)DNA at origins yet must transition to single-stranded (ss)DNA for helicase action. CMG must also handle repair intermediates, such as reversed forks that lack ssDNA. Here, using correlative single-molecule fluorescence and force microscopy, we show that CMG harbors a ssDNA gate that enables transitions between ss and dsDNA. When coupled to DNA polymerase, CMG remains on ssDNA, but when uncoupled, CMG employs this gate to traverse forked junctions onto dsDNA. Surprisingly, CMG undergoes rapid diffusion on dsDNA and can transition back onto ssDNA to nucleate a functional replisome. The gate—distinct from that between Mcm2/5 used for origin loading—is intrinsic to CMG; however, Mcm10 promotes strand passage by enhancing the affinity of CMG to DNA. This gating process may explain the dsDNA-to-ssDNA transition of CMG at origins and help preserve CMG on dsDNA during fork repair.

INTRODUCTION

The DNA replication machinery in all forms of life contains a helicase at the prow of the replication fork that couples ATP hydrolysis to the separation of parental DNA duplexes (Alberts, 2003). While bacterial and archaeal replicative helicases are homohexameric rings, their eukaryotic counterpart is more complex, consisting of a Mcm2-7 heterohexameric ATPase forming a two-tiered ring and an additional five accessory factors—Cdc45 and the GINS heterotetramer (Sld5, Psf1, Psf2, and Psf3)—that brace the N-terminal tier of the Mcm ring (Costa et al., 2011; Deegan and Diffley, 2016; Ilves et al., 2010; Moyer et al., 2006; O'Donnell and Li, 2018; Yuan et al., 2016). This tightly assembled 11-subunit complex is referred to as CMG (Cdc45, Mcm2-7, GINS) (Ilves et al., 2010).

CMG formation occurs at origins of replication and is mediated by a multitude of factors (Bell and Labib, 2016). Helicase loading and activation are segregated into two phases of the cell cycle to ensure that no origin can be fired more than once per cell cycle (Siddiqui et al., 2013). In G1 phase, the origin recognition complex (ORC), Cdc6, and Cdt1 assemble two Mcm2-7 ring hexamers around origin double-stranded (ds)DNA through the Mcm2/5 interface (Bochman and Schwacha, 2008; Samel et al., 2014; Ticau et al., 2017). In S phase, Sld3, Sld7, Sld2, Dpb11, and DNA polymerase Pol ε assemble Cdc45 and GINS onto each Mcm2-7 of the double hexamer. These assembly steps are controlled by two cell-cycle-regulated kinases, CDK and DDK, and result in two CMGs that are oriented on dsDNA in a head-to-head manner (Douglas et al., 2018; Georgescu et al., 2017). The final stage of origin activation requires melting of the origin dsDNA and opening of the two Mcm2-7 rings to encircle opposite single-stranded (ss)DNAs. This transition enables the two CMGs to move past one another, after which they nucleate assembly of replisome components and establish two diverging replication forks. The essential Mcm10 protein is required for CMGs to leave the origin (Baxley and Bielinsky, 2017), possibly by enabling transition from dsDNA to ssDNA. However, the mechanism by which the topologically closed CMG switches from dsDNA to ssDNA binding and the exact role of Mcm10 in CMG activation remain enigmatic.

Once underway, CMG resides at the ss-ds DNA forked junction, unwinding dsDNA by tracking along the leading ssDNA strand in the 3′-to-5′ direction while excluding the lagging strand from its central channel (Fu et al., 2011; Kang et al., 2012; Moyer et al., 2006). Duplication of the leading and lagging strands is carried out by DNA polymerases Pol ε and Pol δ, respectively (Georgescu et al., 2015; Nick McElhinny et al., 2008). During normal synthesis, CMG associates with the polymerases, as well as various other factors, and acts as the central scaffold of the replisome progression complex (Gambus et al., 2006). Analogous to its assembly, disassembly of CMG is also a highly regulated process (Dewar and Walter, 2017). When two opposing forks converge upon replication termination, CMG is ubiquitylated and subsequently unloaded from DNA (Deegan et al., 2019; Maric et al., 2014).

Regular fork progression is often interrupted by DNA damage, recombination intermediates, and other obstacles existing in the chromosome (Berti and Vindigni, 2016). Upon encountering a lesion, Pol ε stalls and uncouples from CMG, and the helicase

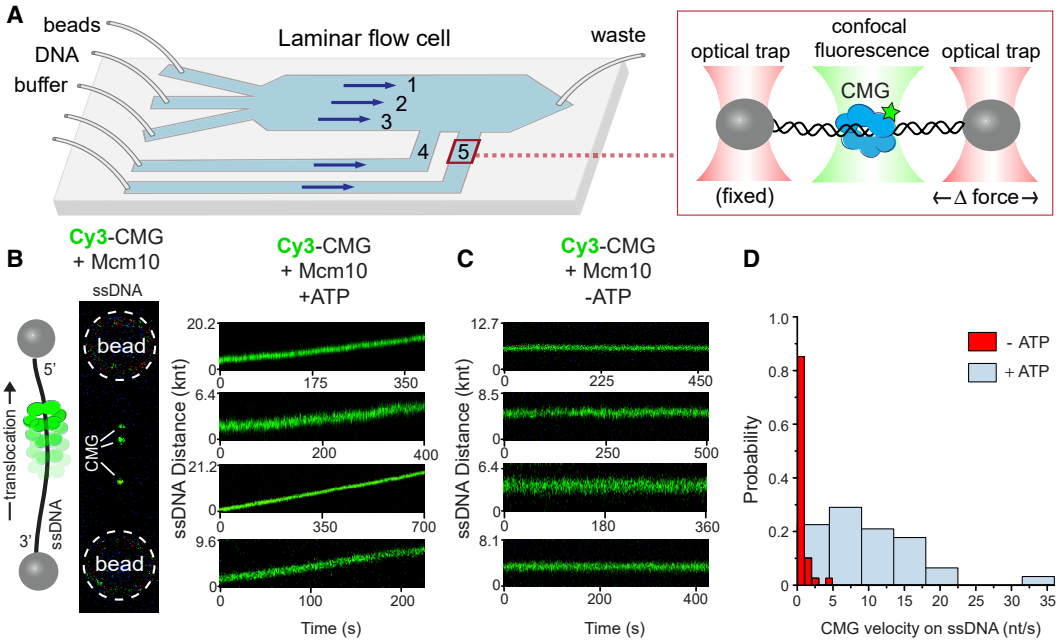

Figure 1. CMG Undergoes Directional Translocation on ssDNA

(A) Schematic of the experimental setup. Individual DNA tethers were formed in channels 1–3 separated by laminar flow containing streptavidin-coated beads, biotinylated λ-DNA, and buffer, respectively. They were subsequently moved to orthogonal channels 4 and 5 for protein loading and imaging. The illustration in the zoom-in box was not drawn to scale.

(B) (Left) Cartoon and 2D scan of a tethered ssDNA loaded with multiple Cy3-CMGs. (Right) Representative kymographs of CMG movement in the presence of 1 mM ATP and 10 nM Mcm10 under 5 pN of tension.

(C) Representative kymographs of Cy3-CMG (green) on ssDNA in the presence of Mcm10 but without ATP.

(D) Distribution of CMG translocation rates on ssDNA in the absence (red) and presence (blue) of ATP (n = 40 and 62, respectively).

See also Figures S1 and S2.

needs to vacate the replication fork so that repair factors can gain access. Moreover, damaged forks can collapse and undergo fork reversal, in which the two nascent daughter strands pair and push the forked nexus backward to form a fourth arm, a structure incompatible with CMG encircling ssDNA (Amunugama et al., 2018; Bhat and Cortez, 2018). The fate of CMG during fork stalling and reversal has not been investigated. Moreover, if CMG dissociates from DNA during repair, it is presumed incapable of rebinding DNA, and therefore, replication restart must await a fork from another origin. However, it remains unclear if CMG can remain on DNA during repair of a fork or if restart always requires another replisome traveling from a neighboring origin.

In this work, we used correlative single-molecule fluorescence and force microscopy to directly observe the behavior of individual CMGs on DNA substrates. We found that CMG possesses the ability to open its closed ring and load onto ssDNA. Following successful ssDNA loading, CMG undergoes unidirectional translocation. Mcm10 promotes this process by enhancing the affinity of CMG to DNA. Furthermore, CMG-Mcm10 can assemble onto a ss-ds DNA fork junction and mediate fork progression and DNA replication. Unexpectedly, we discovered that when uncoupled from an active replisome, CMG-Mcm10 can depart a DNA fork and switch to a rapidly diffusive mode on dsDNA. Upon encountering a new fork, the diffusing CMG can switch back to ssDNA and nucleate a replisome. Together, these results reveal the existence of a ssDNA gate in CMG, which may enable the ring helicase to vacate the fork under replication stress and quickly restart DNA synthesis following repair. The presence of a ssDNA gate in CMG, and the requirement of Mcm10 for robust ss-ds switching, are also uniquely qualified to explain how CMG may transition from encircling dsDNA to encircling ssDNA at an origin.

RESULTS

Directed Motion of CMG on Single-Stranded DNA

We prepared *Saccharomyces cerevisiae* CMG labeled with a Cy3 fluorophore on Cdc45 (Figure S1). We then used a single-molecule instrument that combines confocal fluorescence microscopy, optical tweezers, and automated microfluidics (Hashemi Shabestari et al., 2017) to follow the interaction of CMG with DNA in real time (Figure 1A; STAR Methods). We first examined CMG on a ssDNA substrate prepared from biotinylated phage λ genomic dsDNA (48.5 kilobase pairs [kbp] in length) and tethered between two optically trapped beads (Figures S2A and S2B). We found that, when supplemented with ATP and Mcm10, CMG can readily bind to ssDNA and exhibit unidirectional translocation (Figure 1B). The rate of CMG translocation was measured to be 10.4 ± 0.9 nt/s (mean ± SEM, n = 62) with 1 mM ATP at room temperature. CMG moves

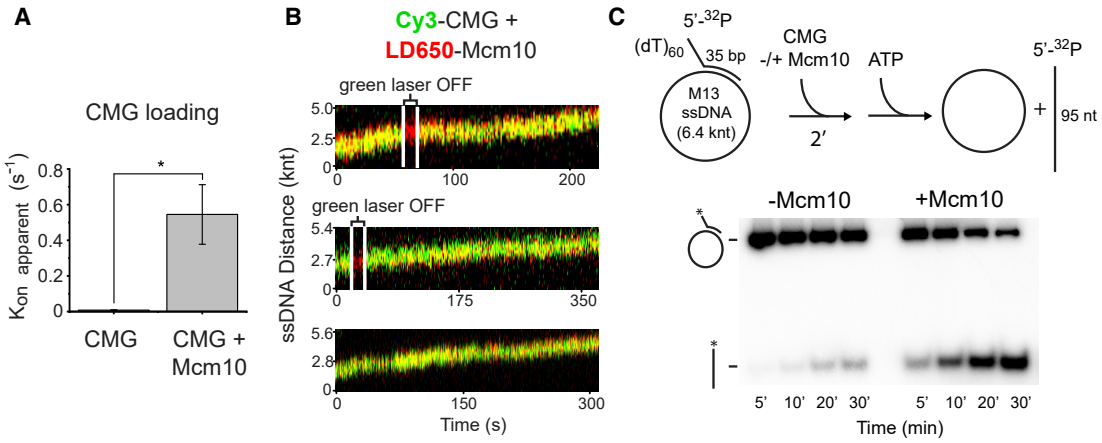

Figure 2. Mcm10 Greatly Stimulates CMG Loading onto ssDNA

(A) Comparison of CMG loading efficiencies in the absence and presence of Mcm10 ($p = 0.0296$), estimated from the number of CMGs stably loaded per unit time at a sub-saturating concentration. Error bars represent SEM generated via bootstrapping.

(B) Representative kymographs demonstrating co-migration of CMG (green) and Mcm10 (red) on ssDNA, illuminated by two excitation lasers (532 nm and 638 nm, respectively). The green laser was occasionally turned off to confirm the fluorescence signal from Mcm10.

(C) Bulk helicase assay showing displacement of a 5′-^{32}P oligonucleotide from circular M13 ssDNA in the absence or presence of Mcm10. CMG must encircle the circular strand in order to unwind the 5′-^{32}P oligonucleotide. Reactions were stopped at the indicated time points.

See also Figures S1 and S2.

on ssDNA in a 3′-to-5′ direction, as confirmed by determining the tether orientation with an oligo probe (Figure S2C; Table S1). The velocity distribution shows a single peak, and no obvious pausing was observed (Figures S2D–S2F). In the absence of ATP, CMG is able to bind but remains stationary on ssDNA (Figures 1C and 1D). Such ATP-dependent directed movement most likely requires strand encirclement via interactions between DNA and the central pore of the Mcm2-7 ring, as supported by structural studies of CMG and replicative hexameric helicases of all cell types (O'Donnell and Li, 2018; O'Shea and Berger, 2014). Moreover, loaded CMG can withstand high salt (0.5 M NaCl) and high tether tension (>80 piconewton [pN]) (Figure S2G), further suggesting that it is topologically linked to ssDNA. These results provide direct evidence that CMG can bind and encircle ssDNA without a free end and translocate in a directional and processive manner, suggesting the existence of a "ssDNA gate" in CMG that allows strand passage.

Mcm10 Is Essential for Efficient CMG Loading onto ssDNA

Next, we assessed the role of Mcm10 in CMG interaction with ssDNA. We found that omission of Mcm10 dramatically decreased the loading efficiency of CMG on ssDNA by 65-fold (Figure 2A) and moderately reduced the speed of CMG movement by 2-fold (5.2 ± 1.6 nt/s, n = 15). These results suggest that Mcm10 plays a critical role in the ability of CMG to encircle and translocate on ssDNA, presumably by forming a complex with CMG. To test this idea, we labeled Mcm10 with an LD650 fluorophore and used dual-color imaging to simultaneously detect CMG and Mcm10 fluorescence signals. Indeed, we observed that CMG and Mcm10 co-localize and co-migrate on ssDNA (Figure 2B). We also performed a bulk helicase assay to corroborate the single-molecule data. Without Mcm10, CMG can unwind a ^{32}P-oligonucleotide with a 5′ flap annealed to circular M13 ssDNA (Ilves et al., 2010; Kang et al., 2012; Langston et al., 2014). Here, we found that Mcm10 significantly stimulates the unwinding activity of CMG (Figure 2C). Due to the 3′-5′ unwinding polarity of CMG, the helicase must open and close to load and encircle the circular ssDNA in order to unwind this flap.

We also examined the interaction of LD650-Mcm10 with ssDNA and found that Mcm10 alone can stably bind DNA but does not display directed motion (Figure S2H). Taken together, these single-molecule and bulk results demonstrate the existence of an intrinsic ssDNA gate in the CMG ring that enables strand passage. Moreover, Mcm10 greatly promotes CMG loading, likely by enhancing its affinity to DNA. Thus, unless noted otherwise, Mcm10 was included throughout this study, and we hereafter refer to the CMG-Mcm10 complex as CMGM.

Loading of CMGM onto DNA Fork Junctions

We next examined the behavior of CMGM on dsDNA. CMGM in solution displayed minimal affinity to a tethered phage λ dsDNA at low force; by contrast, CMGM binding was readily observed upon application of high tension (>65 pN) to the tether (Figure 3A). We posited that this is due to binding of CMGM to force-induced ssDNA regions. To confirm this interpretation, we used the eukaryotic ssDNA-binding protein RPA labeled with Alexa Fluor 488 (A488) to mark ssDNA regions of the tether. Areas of RPA fluorescence emerged when high tension was applied to the tether (Figure 3B), indicating that stretches of dsDNA are melted into ssDNA as characterized previously (King et al., 2013; van Mameren et al., 2009). Notably, lowering the tension back to 10 pN led to strand reannealing and ejection of RPA from DNA, which is demonstrated by disappearance of the RPA fluorescence signal (Figure 3B). The observation that RPA rapidly dissociates in favor of DNA rehybridization entails that RPA alone

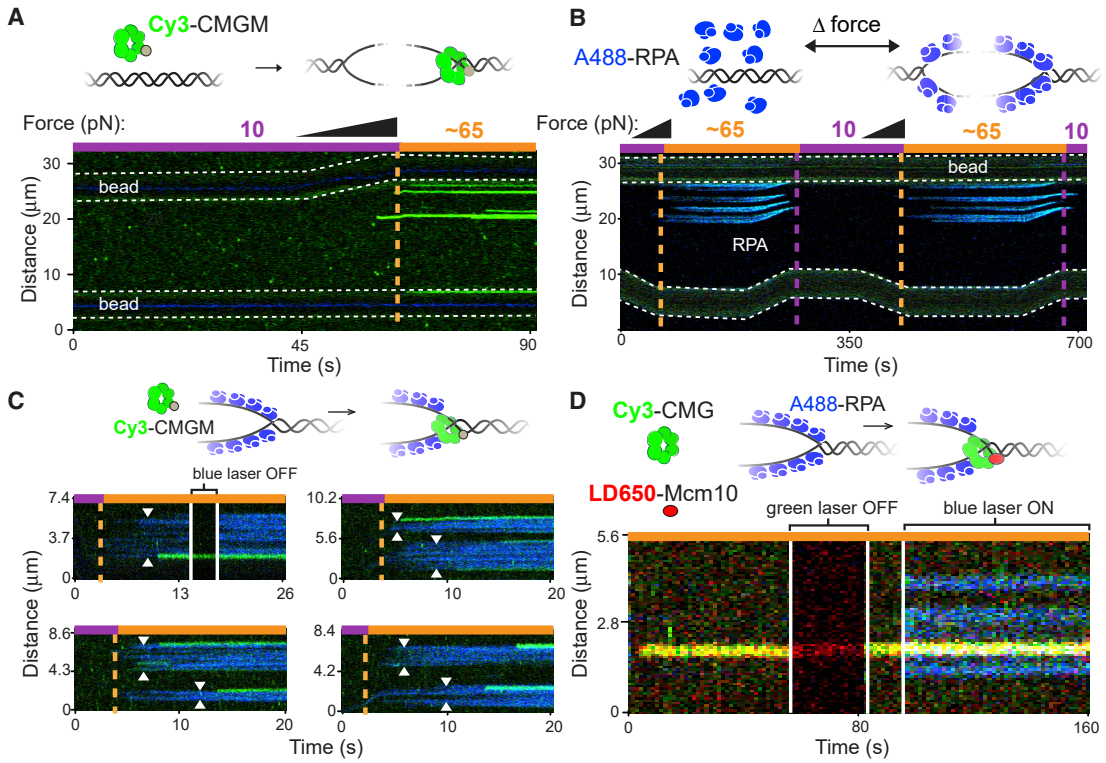

Figure 3. CMGM Loads onto an RPA-Coated DNA Fork

(A) Binding of CMGM (green) to a dsDNA tether is minimal at low force, but greatly enhanced at high force. During the force ramp, one bead held by a movable optical trap is pulled further apart from the other bead held by a fixed trap.

(B) Reversible formation and collapse of ssDNA regions—marked by fluorescently labeled RPA (blue)—via force manipulation of a dsDNA tether.

(C) CMGM preferentially binds near ss-ds fork junctions. Arrows indicate edges of ssDNA regions marked by RPA.

(D) Co-localization of CMG (green) and Mcm10 (red) on RPA-coated ssDNA (blue). Specified lasers were turned on or off to confirm each fluorescence signal. See also Figure S1.

cannot keep two complementary ssDNA strands separated unless the chromosome is under high tension or at least one strand is occupied with other proteins or nucleic acids—a concept that may have important implications for transactions involving RPA-ssDNA during repair or recombination and/or in signaling the DNA damage response.

We then used two-color fluorescence detection to directly analyze the co-localization of Cy3-CMGM and A488-RPA. We found that CMGM preferentially (82%, n = 71) binds near the edges of RPA-coated ssDNA regions (i.e., within ~300 nm or ~500 nt of ss-ds DNA junctions given the spatial resolution of our assay; Figure 3C). We further performed three-color experiments to concomitantly visualize A488-RPA, Cy3-CMG, and LD650-Mcm10 and showed that CMGM stably interacts with RPA-coated ssDNA (Figure 3D).

CMGM Loading at the Fork Leads to Active Replication

The ss-ds DNA junctions formed by force stretching mimic replication forks. If the loaded CMGM encircles ssDNA at the forked junction and functions as a replicative helicase, it is expected to support replisome assembly and DNA synthesis. To test this, we complemented Cy3-CMGM with the numerous protein factors required for replisome-mediated DNA synthesis *in vitro* (STAR Methods) (Georgescu et al., 2015; Lewis et al., 2017). Force was raised to ~65 pN to create single-stranded regions and promote CMGM loading at the fork and subsequently reduced to favor nucleotide addition over exonucleolysis by the polymerase (Wuite et al., 2000). The tethered replication assembly was incubated with a full set of nucleotides and a small amount of digoxigenin-conjugated deoxyuridine triphosphate (Dig-dUTP) and then moved to a separate channel containing Cy5-labeled anti-digoxigenin antibodies (Cy5-anti-Dig; Figure S3A). Importantly, newly synthesized DNA stripes stained by Cy5-anti-Dig were observed, and they were almost exclusively located at positions where Cy3-CMGM loading occurred (91%, n = 46; Figures 4A and S3B). Because Dig-dUTP inhibits the rate of synthesis even when used at a low concentration (Figure S3C), and given the limited time window of our single-molecule measurements, we observed Cy5-anti-Dig tracts no longer than ~1 kb, a diffraction-limited size (~300 nm) of dsDNA at this tension. A similar result was obtained using another modified nucleotide, 5-azidomethyl-dUTP, which can be stained by Cy5-dibenzocyclooctyne (DBCO; Figure S3D).

To seek additional evidence for replisome activity, we supplemented Cy3-CMGM and replisome components with only unmodified nucleotides. In this case, we observed

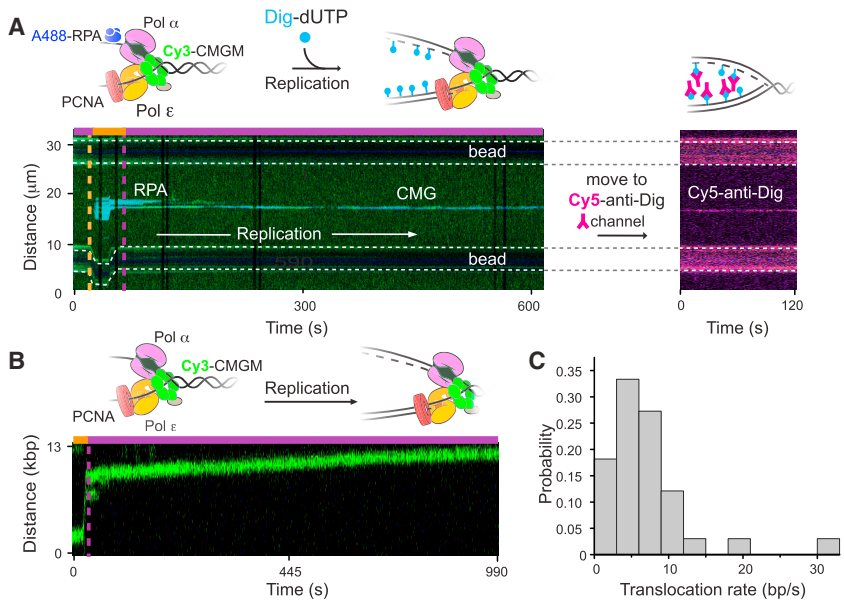

Figure 4. CMGM Loading at the Fork Mediates Replisome Assembly

(A) Representative kymograph demonstrating that CMGM loading at the fork leads to active replication. Cy3-CMGM and other unlabeled replisome components were loaded at a DNA fork marked by A488-RPA in the presence of Dig-dUTP, along with Pol α-primase for priming, Pol ε, replication factor C (RFC), proliferating cell nuclear antigen (PCNA), and Mrc1-Tof1-Csm3 complex. After incubation, the post-replication assembly was moved to a separate channel containing Cy5-anti-Dig for detection of nascent DNA (magenta), which was observed at the same location as CMG.

(B) Representative kymograph showing directed motion of CMGM after binding the fork junction in the presence of unlabeled components required for replication.

(C) Distribution of the velocities of directed motion of CMG upon fork loading (n = 33).

See also Figure S3.

directional movement of the replisome, with a rate of 7.0 ± 1.0 bp/s (mean ± SEM, n = 33) at room temperature (Figures 4B and 4C), consistent with the speed of fork progression measured *in vivo* at 30°C (Sekedat et al., 2010) but one order of magnitude faster than the *in vitro* unwinding rate recently reported using *Drosophila melanogaster* CMG (Burnham et al., 2019). Furthermore, we show in the next section that CMGM, when uncoupled from replisome factors, does not exhibit directional translocation, further supporting that the observed movement is due to replisome progression rather than helicase unwinding. Together, these results strongly suggest that *de novo*-loaded CMGM can lead to replisome assembly and active replication.

CMGM Transitions from ssDNA to dsDNA When Uncoupled from a Polymerase

Next, we sought to follow the fate of CMG once the polymerase becomes uncoupled from the helicase under replication stress. To mimic this situation, we applied the sequential force protocol (high tension followed by low tension) to the dsDNA tether in the presence of only Cy3-CMG and Mcm10 without the other replisome components. Unexpectedly, CMGM was observed to frequently switch to a rapidly diffusive mode upon lowering the force (35%, n = 239), traversing up to tens of kbp of dsDNA (Figure 5A). Mean square displacement analysis showed that this mode of CMGM motion is a random walk, with a diffusion coefficient of 1.66 ± 0.48 kbp^2/s (mean ± SEM, n = 35) at room temperature (Figures 5B–5D).

We interpret this "mode-switch" phenomenon as CMGM transitioning from ssDNA to dsDNA, again necessitating opening of the ssDNA gate in CMG to pass one strand. This interpretation was validated using A488-RPA to distinguish ssDNA from dsDNA. When force was lowered, RPA-bound ssDNA regions reannealed to form duplexes, and CMGM originally residing at the fork junction departed the fork and underwent diffusion (Figure 5E). This ssDNA-to-dsDNA transition relieves CMG from the helicase-unwinding mode and limits the accumulation of ssDNA that is prone to damage.

Previous studies suggest that CMG (Langston and O'Donnell, 2017) and Mcm2-7 hexamer (Evrin et al., 2009; Randell et al., 2006; Remus et al., 2009) are able to encircle and slide over dsDNA. Therefore, we presume that the rapidly diffusive CMGM is topologically linked to dsDNA. This is supported by the observation that diffusion persisted after high-salt wash (Figure S4A) and application of an orthogonal hydrodynamic force (Figure S4B). Nevertheless, we do not rule out the possibility that CMGM may be diffusing on the surface of dsDNA instead of encircling it. In either case, mode switching from ssDNA to dsDNA requires the ssDNA gate to open to either accept the complementary strand or to expel the original strand.

Diffusing CMGM Can Re-enter a Fork to Restart Replication

Upon reintroduction of ssDNA regions by applying high tension again, the rapidly diffusive CMGM soon located a newly formed ss-ds fork junction, at which diffusion halted (Figure 5F). Importantly, when moved to another channel containing free replisome components in solution, a CMGM in the diffusive mode can transition back to the ssDNA-binding mode and recover directed and processive movement characteristic of replisome progression (Figure 5G). This result indicates that the same CMGM that has left the fork junction is able to scan along DNA, re-enter a fork, and assemble an active replisome.

Mcm10 Is Required for CMG Mode Switching

Next, we examined the function of Mcm10 in the transition of CMG from ssDNA to dsDNA. Remarkably, when Mcm10 was omitted from the assay, the vast majority of CMGs (90%, n = 225) dissociated from DNA after collapse of the ss-ds fork junction (Figure 6A) and the mode-switching probability decreased

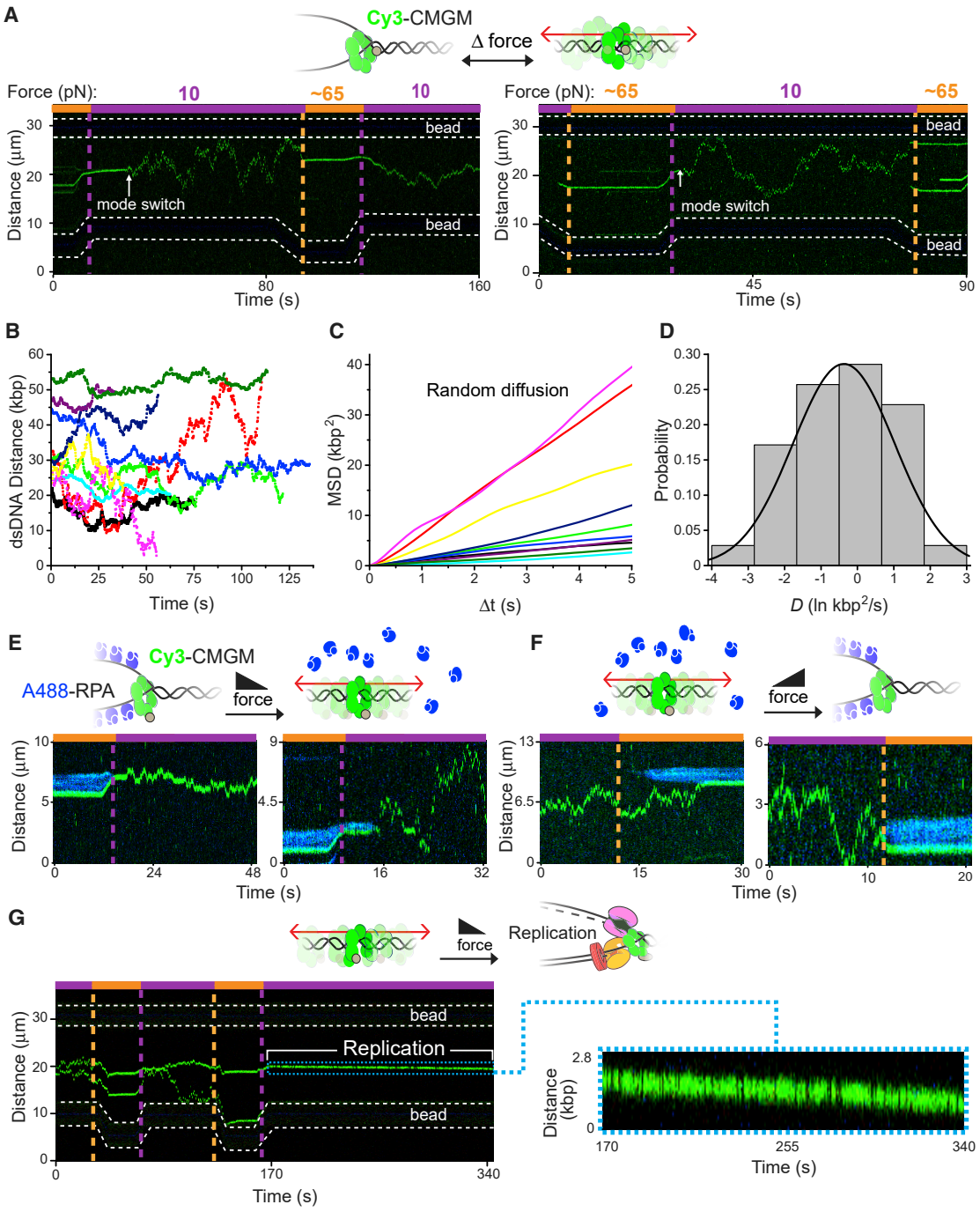

Figure 5. CMGM Transitions Between ssDNA- and dsDNA-Binding Modes in the Absence of Other Replisome Components

(A) Representative kymographs of CMGM (green) switching between non-diffusive (high-force) and diffusive (low-force) modes.

(B) Example trajectories of CMGM in the diffusive mode (offset for clarity).

(C) Mean square displacement (MSD) analysis of the trajectories shown in (B) (color matched). The linear dependence of MSD on Δt suggests that the motion is a random walk.

(D) Distribution of diffusion coefficients (D) estimated by linear regression of the MSD plots from diffusive CMGM trajectories (n = 35). The histogram is fit to a lognormal distribution.

(E and F) Representative kymographs displaying CMGM mode switching at ss-ds fork junctions upon lowering (E) or increasing (F) the tether tension. RPA (blue) was used to distinguish ssDNA from dsDNA regions.

(G) Representative kymograph demonstrating that a diffusive CMGM re-entering a fork in the presence of replisome factors leads to directed translocation. See also Figure S4.

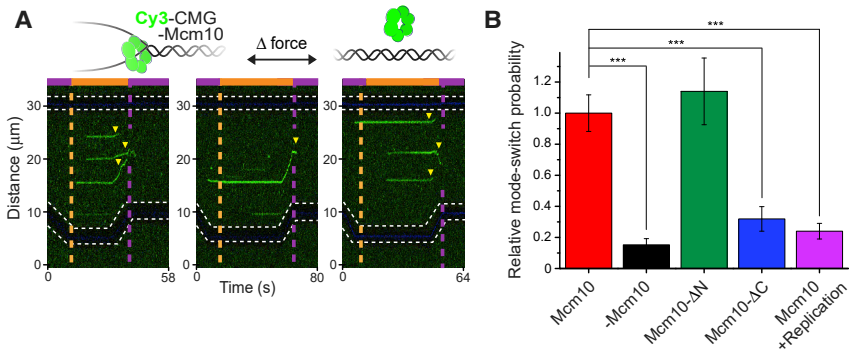

Figure 6. Mcm10 Is Required for Robust CMG Mode Switching from ssDNA to dsDNA

(A) Representative kymographs showing that, in the absence of Mcm10, CMG (green) predominantly dissociates from DNA following fork collapse. Dissociation events are indicated by triangles.

(B) Relative mode-switching probability of CMG in the presence or absence of full-length Mcm10 ($p = 6.2 \times 10^{-7}$), in the presence of Mcm10-ΔN ($p = 0.5626$), Mcm10-ΔC ($p = 2.5 \times 10^{-4}$), or additional replisome components ($p = 5.9 \times 10^{-9}$). Error bars represent SEM.

See also Figures S5 and S6.

drastically (Figure 6B). Thus, as with the Mcm10-dependent loading of CMG onto ssDNA (Figure 2A), Mcm10 is also essential for CMG's robust transition to the diffusive mode and its preservation on dsDNA, again plausibly by enhancing the affinity of CMG to DNA. Indeed, a two-color experiment with Cy3-CMG and LD650-Mcm10 showed that they travel together on dsDNA (Figure S5A). It is noteworthy that, in the presence of replisome components, CMGM persisted at the fork and rarely entered the diffusive mode (Figures 4B and 6B), indicating that disengagement of CMGM from an actively synthesizing polymerase substantially stimulates CMGM's transition from ssDNA to dsDNA.

To further dissect the role of Mcm10 in CMG mode switching, we generated two truncated versions of Mcm10—an N-terminal deletion (Mcm10-ΔN) and a C-terminal deletion (Mcm10-ΔC) (Figure S5B). Previous work showed that Mcm10-ΔC does not support yeast survival, whereas Mcm10-ΔN confers no growth defects (Lõoke et al., 2017). Interestingly, we found that, upon force reduction, CMG-Mcm10-ΔN transitions to the diffusive mode with a similar efficiency compared to the full-length Mcm10 (Figures 6B, S5C, and S5E). In contrast, the mode-switching probability is significantly decreased for Mcm10-ΔC to a level similar to the no-Mcm10 condition (Figures 6B, S5D, and S5E). Thus, the function of these Mcm10 mutants to support CMG mode-switching *in vitro* correlates with cellular viability of these mutants *in vivo*, indicating that the ability of CMG to open its ssDNA gate and switch to a diffusive mode on dsDNA—with the help of Mcm10—is a physiologically relevant activity.

The Mcm2/5 Interface Is Not the ssDNA Gate of CMG

The transitions between ssDNA and dsDNA binding modes of CMG require opening of the Mcm2-7 ring to pass a strand either into the central channel or out of it. The Mcm2/5 interface is used for loading Mcm2-7 around dsDNA during origin licensing (Samel et al., 2014; Ticau et al., 2017); however, this interface is occluded by Cdc45 and GINS in the CMG complex (Costa et al., 2011). We therefore sought to examine whether this demonstrated gate is also used for ssDNA gating. To this end, we employed CRISPR-Cas to engineer a yeast strain that produces CMG harboring a previously demonstrated rapamycin-inducible linkage between Mcm2 and Mcm5 (Figures S6A and S6B; STAR Methods) (Samel et al., 2014). Both ssDNA-loading and mode-switching analyses showed similar results in the presence and absence of a sealed Mcm2/5 interface (Figures S6C–S6E). Therefore, for ssDNA gating, CMG either uses a different interface in the Mcm2-7 ring or employs multiple interfaces.

DISCUSSION

It has been widely accepted that the assembly and disassembly of CMG—the eukaryotic replicative helicase conserved from yeast to humans—are restricted to specific cell-cycle stages and are tightly regulated by other factors (Bell and Labib, 2016). In this work, by creating DNA forks *in situ* via force manipulation, observing the behavior of single CMG complexes via fluorescence detection, and subjecting the replisome assembly to different reaction mixtures via microfluidic control, we found that CMG displays an unexpected degree of structural and functional plasticity. Our results showed directed motion of CMG on ssDNA and its random diffusion on dsDNA, and revealed that CMG can reversibly switch between these distinct DNA-binding modes. When uncoupled from a polymerase as expected under replication stress, CMG-Mcm10 can transition from ssDNA to dsDNA, which provides a mechanism for CMG to vacate a stalled fork while remaining stored on dsDNA. The reverse mode-switch—from dsDNA to ssDNA—allows CMG to re-engage the fork to resume replication (Figure 7A). We further demonstrated that Mcm10 is essential for these transitions and remains associated with CMG during the ssDNA-gating events. In addition, the ssDNA gate in CMG documented here would also explain the Mcm10-dependent CMG transition from dsDNA onto ssDNA at an origin (Figure 7B; discussed in more detail below).

Molecular Mechanism of ssDNA Gating by CMG

It can be inferred from earlier data that CMG possesses an intrinsic ssDNA gate, as CMG alone can strip a 5′ tailed oligo from circular ssDNA (Ilves et al., 2010; Kang et al., 2012; Langston et al., 2014). The present work provides the first visual evidence that CMG encircles and directionally translocates on ssDNA without any free end, necessitating opening of the Mcm2-7 ring. It is unlikely that CMG is constitutively open because all the available structures of CMG display a closed topology (reviewed in Li and O'Donnell, 2018). Hence, the ssDNA gate in Mcm2-7 must only open transiently. However, the

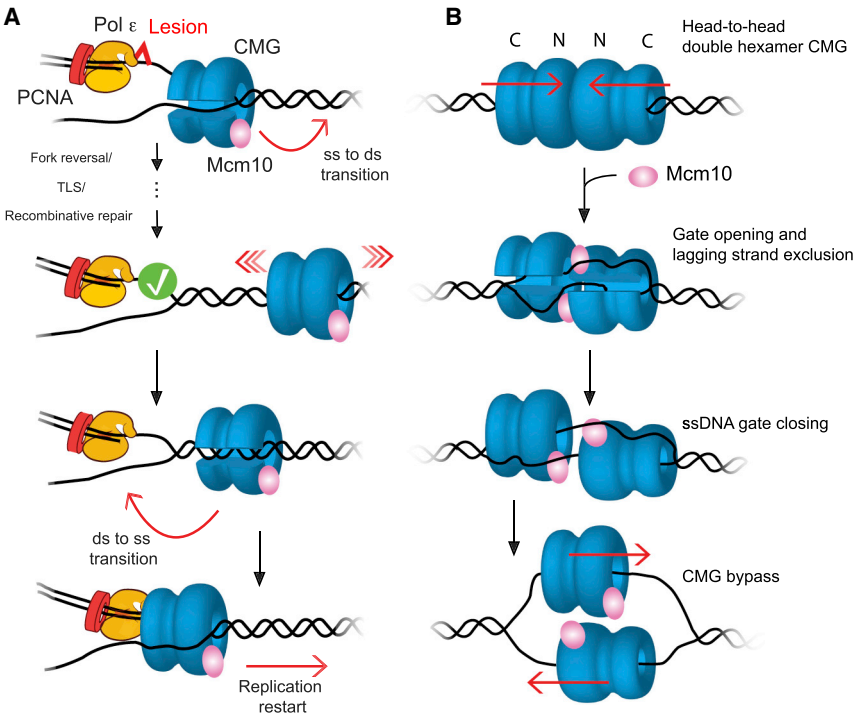

Figure 7. Implications of CMG ssDNA Gating in Replisome Preservation and Origin Firing

(A) CMG-Mcm10 uncouples from the polymerase and transitions from ssDNA to dsDNA when the replisome stalls during replication stress, for example upon encountering a lesion (red symbol). Upon decoupling, CMGM opens the ssDNA gate and transitions to a fast diffusive mode on dsDNA. Meanwhile, lesions are repaired (green symbol) through a multitude of stress-response pathways available to the cell. When the stress response is complete, CMGM can re-enter the fork by transitioning from dsDNA to ssDNA. CMGM nucleates replisome assembly at the restored fork, leading to replication restart.

(B) Licensed double-hexamer CMGs are oriented in a head-to-head (N-to-N) fashion. The ssDNA gate in CMG enables lagging strand exclusion followed by gate closing. Only when each CMG is loaded onto its respective leading strand may they bypass each other and mutually fire. Mcm10 is required for robust ssDNA gating and replication initiation.

See also Figure S7.

opened conformation of CMG appears to have a low affinity to DNA, as reflected by its poor ssDNA loading efficiency by itself, which is drastically enhanced by the presence of Mcm10. Likewise, when CMG lacking Mcm10 opens its ssDNA gate at a collapsed replication fork, it predominantly dissociates into solution. Mcm10 significantly increases the likelihood of CMG transitioning to the dsDNA-binding, diffusive mode.

These mutually consistent results suggest a model in which a transiently opened form of CMG is tethered to DNA through Mcm10, likely mediated by its known DNA binding domains (Warren et al., 2008). The reclosure of the Mcm2-7 ring on DNA does not seem to require Mcm10, because in the few cases when CMG alone avoided dissociation, it underwent directional translocation on ssDNA and diffusive movement on dsDNA similar to CMGM. Thus, the most parsimonious mechanism to explain the Mcm10 effect is that it holds CMG on DNA, taking advantage of an intrinsic ssDNA gate in CMG for loading onto ssDNA and mode switching onto dsDNA (Figure S7). While we cannot exclude the possibility that Mcm10 may also modulate the gating kinetics of CMG, such a mechanism is not needed to interpret our results.

Paradoxically, the ssDNA gating of CMG adopts a distinct mechanism from the dsDNA gating process by the same Mcm2-7 ring. During dsDNA loading of Mcm2-7, the Mcm2/5 interface is constitutively open—stabilized by Cdt1 (Frigola et al., 2017; Zhai et al., 2017)—and closed by hydrolysis of ATP for duplex encirclement (Bleichert et al., 2017; Ticau et al., 2017). In agreement with this distinction, we showed that prevention of Mcm2/5 gate opening has little effect on the ability of CMGM to load onto ssDNA or to transition from ssDNA to dsDNA, even though it abolishes Mcm2-7 loading during pre-replicative complex formation (Samel et al., 2014). This result was anticipated from the occlusion of the 2/5 gate by Cdc45/GINS, shown to help retain CMG on DNA during its function at a replication fork (Petojevic et al., 2015).

Biological Implications of ssDNA Gating by CMG

The ssDNA gate in CMG has several important implications in DNA replication and repair. First, the ssDNA gate in CMG may be employed for bypassing certain DNA lesions. Recent work using *Xenopus* egg extracts concluded that CMG can traverse a covalently bound protein roadblock (Sparks et al., 2019). While metazoan CMG may have unique properties compared to yeast CMG, the ssDNA gating process demonstrated here offers a plausible mechanism to explain how CMG deals with various DNA lesions, including bulky adducts and DNA-protein crosslinks.

Replication stress can induce various DNA recombination intermediates that are essential for the damage response but incompatible with retaining a replisome at the fork (Sidorova, 2017; Sogo et al., 2002). Fork reversal represents one such scenario (Bhat and Cortez, 2018). Single-molecule studies in the phage T4 system indicate that the replicative helicase is removed from the fork during reversal (Manosas et al., 2012). However, whether CMG is similarly unloaded from the fork was unknown. Our data suggest that CMG uses its ssDNA gate to jump the fork (i.e., pass the lagging strand). CMG may scan along the dsDNA downstream of the four-way junction of a reversed fork, where it could wait out the repair and restoration of reversed forks. Another possibility is that CMG may be stored on the nascent DNA duplex, in which case it could facilitate fork restoration by catalyzing branch migration.

How a repaired fork is restarted is another key question. Prokaryotic systems have evolved mechanisms of reloading

the replicative helicase onto the ssDNA of an empty fork for reactivation (Marians, 2018). The occurrence and necessity of helicase reloading in eukaryotic cells has been unclear and somewhat de-emphasized given the existence of dormant licensed origins. It is generally thought that a eukaryotic fork can only be restarted by recruiting a new CMG from a nearby origin. The present work suggests another pathway for CMG diffusing on dsDNA to re-enter a fork via its ssDNA gate and assemble a new replisome. Note that it takes CMG much less time to cover the same distance between adjacent origins via diffusion (~1.7 kbp^2/s) than through normal fork progression (~25 bp/s) (Sekedat et al., 2010). Furthermore, considering that most of the eukaryotic genome is packaged into nucleosomes—which could act as barriers to CMG diffusion—it is anticipated that CMG is kept in close proximity to the fork that it departed from. Therefore, temporarily transferring CMG to dsDNA is likely a more efficient strategy for the cell to rapidly recover replication following repair. We refer to this mechanism as "replisome preservation" because CMGM itself can nucleate a replisome *de novo* by recruiting soluble replication components.

Importantly, ssDNA gating is required at the last stages of origin initiation (Figure 7B). Here, two CMGs are assembled head to head around dsDNA at origins with their N termini facing each other (Evrin et al., 2009; Remus et al., 2009). Given the N-first tracking direction of CMG, each CMG must transition from dsDNA to opposite strands of ssDNA to pass one another, as suggested by work from our group (Georgescu et al., 2017) and others (Douglas et al., 2018). Thus, at an origin, CMG must pass the non-tracking strand to the exterior—possibly through the ssDNA gate documented here—in order for the two CMGs to move past one another and establish bidirectional replication. While the process that initially melts DNA at the origin is unknown, Mcm10, the final origin-firing factor, is essential during these steps leading to replication elongation (Heller et al., 2011; Kanke et al., 2012; van Deursen et al., 2012; Watase et al., 2012). The Mcm10 function in ssDNA gating documented here may directly explain this critical aspect of replication initiation.

Finally, it was shown that CMG on dsDNA can be ubiquitylated and proteolyzed in certain genomic contexts, such as replication termination and interstrand crosslink repair (Dewar et al., 2017; Sonneville et al., 2017). One may question whether mode switching observed here would trigger similar pathways that remove CMG from DNA. However, such programmed disassembly of CMG mainly takes place outside the bulk of S phase and is activated by specific cellular signals such as fork convergence and mitotic entry (Deng et al., 2019; Wu et al., 2019). On the other hand, the uncoupling of CMG from DNA polymerase, which we show triggers the transition of CMG to the diffusive mode on dsDNA, is expected to happen during S phase under replication stress. Therefore, the ubiquitylation-dependent irreversible CMG disassembly and the reversible CMG mode switching likely represent distinct mechanisms for CMG to vacate the fork and serve different biological functions that are spatially and temporally segregated. Moreover, it was reported that the ubiquitylation-dependent pathway takes over 20 min for significant amounts of CMG removal (Dewar et al., 2017), making it further unlikely that a CMG diffusing on dsDNA in S phase is disassembled before returning to a fork.

Perspective

In this work, our unique single-molecule platform led to the finding that CMG employs a ssDNA gate for facile strand passage, which provides an attractive solution to several puzzles related to eukaryotic DNA replication and repair. Many important questions emerge in light of these new results. It remains to be seen which other replisome factors are associated with CMGM when it diffuses on dsDNA. Characterization of the roles of checkpoint kinases, such as Mec1 and Rad53, during CMG mode switching between encircling ssDNA and dsDNA will be important for a more complete picture of the replisome preservation process. Identification of the Mcm interface (or multiple interfaces) involved in the gate and the exact role of Mcm10 in CMG ssDNA gating will shed more light on these processes. Such inquiry may be further aided by structural studies of CMGM. It will also be interesting to use biophysical tools such as fluorescence resonance energy transfer (FRET) to directly measure the gating kinetics. Answers to these questions will contribute to a better understanding of how CMGM functions at origins and how it properly responds to DNA damage and replication stress in order to ensure genome integrity and accurate duplication of long chromosomes.

STAR★METHODS

Detailed methods are provided in the online version of this paper and include the following:

- KEY RESOURCES TABLE
- LEAD CONTACT AND MATERIALS AVAILABILITY
- EXPERIMENTAL MODEL AND SUBJECT DETAILS
- METHOD DETAILS
  - Protein purification and labeling
  - DNA Substrate Preparation
  - Bulk Helicase Unwinding Assay
  - Bulk Replication Assay
  - Single-Molecule Experiments
- QUANTIFICATION AND STATISTICAL ANALYSIS
- DATA AND CODE AVAILABILITY

SUPPLEMENTAL INFORMATION

Supplemental Information can be found online at https://doi.org/10.1016/j.cell.2019.06.032.

ACKNOWLEDGMENTS

We thank Drs. Olga Yurieva and Dan Zhang for assistance with protein purification and strain construction and other members of the O'Donnell and Liu laboratories for discussions. This work was supported by a postdoctoral fellowship from the Anderson Cancer Center at The Rockefeller University (to M.R.W.), the Robertson Foundation, the Quadrivium Foundation, a Monique Weill-Caulier Career Award, a Basil O'Connor Starter Scholar Award from the March of Dimes (#5-FY17-61), a Kimmel Scholar Award (to S.L.), the National Institutes of Health (T32 CA009673 and K99 GM126143 to G.D.S., R00 GM107365 and DP2 HG010510 to S.L., and R01 GM115809 to M.E.O.), and the Howard Hughes Medical Institute (to M.E.O.).

AUTHOR CONTRIBUTIONS

S.L. and M.E.O oversaw the project. M.R.W. and G.D.S. performed the experiments and analyzed the data. All authors wrote the manuscript.

DECLARATION OF INTERESTS

The authors declare no competing interests.

Received: July 25, 2018
Revised: April 5, 2019
Accepted: June 24, 2019
Published: July 25, 2019

REFERENCES

Aitken, C.E., Marshall, R.A., and Puglisi, J.D. (2008). An oxygen scavenging system for improvement of dye stability in single-molecule fluorescence experiments. Biophys. J. *94*, 1826–1835.

Alberts, B. (2003). DNA replication and recombination. Nature *421*, 431–435.

Altman, R.B., Terry, D.S., Zhou, Z., Zheng, Q., Geggier, P., Kolster, R.A., Zhao, Y., Javitch, J.A., Warren, J.D., and Blanchard, S.C. (2011). Cyanine fluorophore derivatives with enhanced photostability. Nat. Methods *9*, 68–71.

Amunugama, R., Willcox, S., Wu, R.A., Abdullah, U.B., El-Sagheer, A.H., Brown, T., McHugh, P.J., Griffith, J.D., and Walter, J.C. (2018). Replication Fork Reversal during DNA Interstrand Crosslink Repair Requires CMG Unloading. Cell Rep. *23*, 3419–3428.

Bauer, G.A., and Burgers, P.M. (1988). The yeast analog of mammalian cyclin/proliferating-cell nuclear antigen interacts with mammalian DNA polymerase delta. Proc. Natl. Acad. Sci. USA *85*, 7506–7510.

Baxley, R.M., and Bielinsky, A.K. (2017). Mcm10: A Dynamic Scaffold at Eukaryotic Replication Forks. Genes (Basel) *8*, E73.

Bell, S.P., and Labib, K. (2016). Chromosome Duplication in Saccharomyces cerevisiae. Genetics *203*, 1027–1067.

Berti, M., and Vindigni, A. (2016). Replication stress: getting back on track. Nat. Struct. Mol. Biol. *23*, 103–109.

Bhat, K.P., and Cortez, D. (2018). RPA and RAD51: fork reversal, fork protection, and genome stability. Nat. Struct. Mol. Biol. *25*, 446–453.

Bleichert, F., Botchan, M.R., and Berger, J.M. (2017). Mechanisms for initiating cellular DNA replication. Science *355*, eaah6317.

Bochman, M.L., and Schwacha, A. (2008). The Mcm2-7 complex has in vitro helicase activity. Mol. Cell *31*, 287–293.

Burnham, D.R., Kose, H.B., Hoyle, R.B., and Yardimci, H. (2019). The mechanism of DNA unwinding by the eukaryotic replicative helicase. Nat. Commun. *10*, 2159.

Candelli, A., Hoekstra, T.P., Farge, G., Gross, P., Peterman, E.J., and Wuite, G.J. (2013). A toolbox for generating single-stranded DNA in optical tweezers experiments. Biopolymers *99*, 611–620.

Costa, A., Ilves, I., Tamberg, N., Petojevic, T., Nogales, E., Botchan, M.R., and Berger, J.M. (2011). The structural basis for MCM2-7 helicase activation by GINS and Cdc45. Nat. Struct. Mol. Biol. *18*, 471–477.

Dave, R., Terry, D.S., Munro, J.B., and Blanchard, S.C. (2009). Mitigating unwanted photophysical processes for improved single-molecule fluorescence imaging. Biophys. J. *96*, 2371–2381.

Deegan, T.D., and Diffley, J.F. (2016). MCM: one ring to rule them all. Curr. Opin. Struct. Biol. *37*, 145–151.

Deegan, T.D., Baxter, J., Ortiz Bazan, M.Á., Yeeles, J.T.P., and Labib, K.P.M. (2019). Pif1-Family Helicases Support Fork Convergence during DNA Replication Termination in Eukaryotes. Mol. Cell *74*, 231–244.

Deng, L., Wu, R.A., Sonneville, R., Kochenova, O.V., Labib, K., Pellman, D., and Walter, J.C. (2019). Mitotic CDK Promotes Replisome Disassembly, Fork Breakage, and Complex DNA Rearrangements. Mol. Cell *73*, 915–929.

Dewar, J.M., and Walter, J.C. (2017). Mechanisms of DNA replication termination. Nat. Rev. Mol. Cell Biol. *18*, 507–516.

Dewar, J.M., Low, E., Mann, M., Räschle, M., and Walter, J.C. (2017). CRL2^{Lrr1} promotes unloading of the vertebrate replisome from chromatin during replication termination. Genes Dev. *31*, 275–290.

Douglas, M.E., Ali, F.A., Costa, A., and Diffley, J.F.X. (2018). The mechanism of eukaryotic CMG helicase activation. Nature *555*, 265–268.

Eeftens, J.M., van der Torre, J., Burnham, D.R., and Dekker, C. (2015). Copper-free click chemistry for attachment of biomolecules in magnetic tweezers. BMC Biophys. *8*, 9.

Evrin, C., Clarke, P., Zech, J., Lurz, R., Sun, J., Uhle, S., Li, H., Stillman, B., and Speck, C. (2009). A double-hexameric MCM2-7 complex is loaded onto origin DNA during licensing of eukaryotic DNA replication. Proc. Natl. Acad. Sci. USA *106*, 20240–20245.

Finkelstein, J., Antony, E., Hingorani, M.M., and O'Donnell, M. (2003). Overproduction and analysis of eukaryotic multiprotein complexes in Escherichia coli using a dual-vector strategy. Anal. Biochem. *319*, 78–87.

Frigola, J., He, J., Kinkelin, K., Pye, V.E., Renault, L., Douglas, M.E., Remus, D., Cherepanov, P., Costa, A., and Diffley, J.F.X. (2017). Cdt1 stabilizes an open MCM ring for helicase loading. Nat. Commun. *8*, 15720.

Fu, Y.V., Yardimci, H., Long, D.T., Ho, T.V., Guainazzi, A., Bermudez, V.P., Hurwitz, J., van Oijen, A., Schärer, O.D., and Walter, J.C. (2011). Selective bypass of a lagging strand roadblock by the eukaryotic replicative DNA helicase. Cell *146*, 931–941.

Galburt, E.A., Grill, S.W., and Bustamante, C. (2009). Single molecule transcription elongation. Methods *48*, 323–332.

Gambus, A., Jones, R.C., Sanchez-Diaz, A., Kanemaki, M., van Deursen, F., Edmondson, R.D., and Labib, K. (2006). GINS maintains association of Cdc45 with MCM in replisome progression complexes at eukaryotic DNA replication forks. Nat. Cell Biol. *8*, 358–366.

Georgescu, R.E., Langston, L., Yao, N.Y., Yurieva, O., Zhang, D., Finkelstein, J., Agarwal, T., and O'Donnell, M.E. (2014). Mechanism of asymmetric polymerase assembly at the eukaryotic replication fork. Nat. Struct. Mol. Biol. *21*, 664–670.

Georgescu, R.E., Schauer, G.D., Yao, N.Y., Langston, L.D., Yurieva, O., Zhang, D., Finkelstein, J., and O'Donnell, M.E. (2015). Reconstitution of a eukaryotic replisome reveals suppression mechanisms that define leading/lagging strand operation. eLife *4*, e04988.

Georgescu, R., Yuan, Z., Bai, L., de Luna Almeida Santos, R., Sun, J., Zhang, D., Yurieva, O., Li, H., and O'Donnell, M.E. (2017). Structure of eukaryotic CMG helicase at a replication fork and implications to replisome architecture and origin initiation. Proc. Natl. Acad. Sci. USA *114*, E697–E706.

Hashemi Shabestari, M., Meijering, A.E.C., Roos, W.H., Wuite, G.J.L., and Peterman, E.J.G. (2017). Recent Advances in Biological Single-Molecule Applications of Optical Tweezers and Fluorescence Microscopy. Methods Enzymol. *582*, 85–119.

Heller, R.C., Kang, S., Lam, W.M., Chen, S., Chan, C.S., and Bell, S.P. (2011). Eukaryotic origin-dependent DNA replication in vitro reveals sequential action of DDK and S-CDK kinases. Cell *146*, 80–91.

Henricksen, L.A., Umbricht, C.B., and Wold, M.S. (1994). Recombinant replication protein A: expression, complex formation, and functional characterization. J. Biol. Chem. *269*, 11121–11132.

Ilves, I., Petojevic, T., Pesavento, J.J., and Botchan, M.R. (2010). Activation of the MCM2-7 helicase by association with Cdc45 and GINS proteins. Mol. Cell *37*, 247–258.

Kang, Y.H., Galal, W.C., Farina, A., Tappin, I., and Hurwitz, J. (2012). Properties of the human Cdc45/Mcm2-7/GINS helicase complex and its action with DNA polymerase epsilon in rolling circle DNA synthesis. Proc. Natl. Acad. Sci. USA *109*, 6042–6047.

Kanke, M., Kodama, Y., Takahashi, T.S., Nakagawa, T., and Masukata, H. (2012). Mcm10 plays an essential role in origin DNA unwinding after loading of the CMG components. EMBO J. *31*, 2182–2194.

King, G.A., Gross, P., Bockelmann, U., Modesti, M., Wuite, G.J., and Peterman, E.J. (2013). Revealing the competition between peeled ssDNA, melting bubbles, and S-DNA during DNA overstretching using fluorescence microscopy. Proc. Natl. Acad. Sci. USA *110*, 3859–3864.

Langston, L., and O'Donnell, M. (2017). Action of CMG with strand-specific DNA blocks supports an internal unwinding mode for the eukaryotic replicative helicase. eLife *6*, e23449.

Langston, L.D., Zhang, D., Yurieva, O., Georgescu, R.E., Finkelstein, J., Yao, N.Y., Indiani, C., and O'Donnell, M.E. (2014). CMG helicase and DNA polymerase ε form a functional 15-subunit holoenzyme for eukaryotic leading-strand DNA replication. Proc. Natl. Acad. Sci. USA *111*, 15390–15395.

Langston, L.D., Mayle, R., Schauer, G.D., Yurieva, O., Zhang, D., Yao, N.Y., Georgescu, R.E., and O'Donnell, M.E. (2017). Mcm10 promotes rapid isomerization of CMG-DNA for replisome bypass of lagging strand DNA blocks. eLife *6*, e29118.

Lewis, J.S., Spenkelink, L.M., Schauer, G.D., Hill, F.R., Georgescu, R.E., O'Donnell, M.E., and van Oijen, A.M. (2017). Single-molecule visualization of *Saccharomyces cerevisiae* leading-strand synthesis reveals dynamic interaction between MTC and the replisome. Proc. Natl. Acad. Sci. USA *114*, 10630–10635.

Li, H., and O'Donnell, M.E. (2018). The Eukaryotic CMG Helicase at the Replication Fork: Emerging Architecture Reveals an Unexpected Mechanism. BioEssays *40*, 201700208.

Lõoke, M., Maloney, M.F., and Bell, S.P. (2017). Mcm10 regulates DNA replication elongation by stimulating the CMG replicative helicase. Genes Dev. *31*, 291–305.

Mangeol, P., Prevo, B., and Peterman, E.J. (2016). KymographClear and KymographDirect: two tools for the automated quantitative analysis of molecular and cellular dynamics using kymographs. Mol. Biol. Cell *27*, 1948–1957.

Manosas, M., Perumal, S.K., Croquette, V., and Benkovic, S.J. (2012). Direct observation of stalled fork restart via fork regression in the T4 replication system. Science *338*, 1217–1220.

Marians, K.J. (2018). Lesion Bypass and the Reactivation of Stalled Replication Forks. Annu. Rev. Biochem. *87*, 217–238.

Maric, M., Maculins, T., De Piccoli, G., and Labib, K. (2014). Cdc48 and a ubiquitin ligase drive disassembly of the CMG helicase at the end of DNA replication. Science *346*, 1253596.

Moyer, S.E., Lewis, P.W., and Botchan, M.R. (2006). Isolation of the Cdc45/Mcm2-7/GINS (CMG) complex, a candidate for the eukaryotic DNA replication fork helicase. Proc. Natl. Acad. Sci. USA *103*, 10236–10241.

Nick McElhinny, S.A., Gordenin, D.A., Stith, C.M., Burgers, P.M., and Kunkel, T.A. (2008). Division of labor at the eukaryotic replication fork. Mol. Cell *30*, 137–144.

O'Donnell, M.E., and Li, H. (2018). The ring-shaped hexameric helicases that function at DNA replication forks. Nat. Struct. Mol. Biol. *25*, 122–130.

O'Shea, V.L., and Berger, J.M. (2014). Loading strategies of ring-shaped nucleic acid translocases and helicases. Curr. Opin. Struct. Biol. *25*, 16–24.

Petojevic, T., Pesavento, J.J., Costa, A., Liang, J., Wang, Z., Berger, J.M., and Botchan, M.R. (2015). Cdc45 (cell division cycle protein 45) guards the gate of the Eukaryote Replisome helicase stabilizing leading strand engagement. Proc. Natl. Acad. Sci. USA *112*, E249–E258.

Randell, J.C., Bowers, J.L., Rodríguez, H.K., and Bell, S.P. (2006). Sequential ATP hydrolysis by Cdc6 and ORC directs loading of the Mcm2-7 helicase. Mol. Cell *21*, 29–39.

Remus, D., Beuron, F., Tolun, G., Griffith, J.D., Morris, E.P., and Diffley, J.F. (2009). Concerted loading of Mcm2-7 double hexamers around DNA during DNA replication origin licensing. Cell *139*, 719–730.

Samel, S.A., Fernández-Cid, A., Sun, J., Riera, A., Tognetti, S., Herrera, M.C., Li, H., and Speck, C. (2014). A unique DNA entry gate serves for regulated loading of the eukaryotic replicative helicase MCM2-7 onto DNA. Genes Dev. *28*, 1653–1666.

Schauer, G., Finkelstein, J., and O'Donnell, M. (2017). *In vitro* Assays for Eukaryotic Leading/Lagging Strand DNA Replication. Bio Protoc. *7*, 2548.

Schindelin, J., Arganda-Carreras, I., Frise, E., Kaynig, V., Longair, M., Pietzsch, T., Preibisch, S., Rueden, C., Saalfeld, S., Schmid, B., et al. (2012). Fiji: an open-source platform for biological-image analysis. Nat. Methods *9*, 676–682.

Sekedat, M.D., Fenyö, D., Rogers, R.S., Tackett, A.J., Aitchison, J.D., and Chait, B.T. (2010). GINS motion reveals replication fork progression is remarkably uniform throughout the yeast genome. Mol. Syst. Biol. *6*, 353.

Sélo, I., Négroni, L., Créminon, C., Grassi, J., and Wal, J.M. (1996). Preferential labeling of alpha-amino N-terminal groups in peptides by biotin: application to the detection of specific anti-peptide antibodies by enzyme immunoassays. J. Immunol. Methods *199*, 127–138.

Siddiqui, K., On, K.F., and Diffley, J.F. (2013). Regulating DNA replication in eukarya. Cold Spring Harb. Perspect. Biol. *5*, a012930.

Sidorova, J. (2017). A game of substrates: replication fork remodeling and its roles in genome stability and chemo-resistance. Cell Stress *1*, 115–133.

Smith, S.B., Cui, Y., and Bustamante, C. (1996). Overstretching B-DNA: the elastic response of individual double-stranded and single-stranded DNA molecules. Science *271*, 795–799.

Sogo, J.M., Lopes, M., and Foiani, M. (2002). Fork reversal and ssDNA accumulation at stalled replication forks owing to checkpoint defects. Science *297*, 599–602.

Sonneville, R., Moreno, S.P., Knebel, A., Johnson, C., Hastie, C.J., Gartner, A., Gambus, A., and Labib, K. (2017). CUL-2^{LRR-1} and UBXN-3 drive replisome disassembly during DNA replication termination and mitosis. Nat. Cell Biol. *19*, 468–479.

Sparks, J.L., Chistol, G., Gao, A.O., Räschle, M., Larsen, N.B., Mann, M., Duxin, J.P., and Walter, J.C. (2019). The CMG Helicase Bypasses DNA-Protein Cross-Links to Facilitate Their Repair. Cell *176*, 167–181.

Tarantino, N., Tinevez, J.Y., Crowell, E.F., Boisson, B., Henriques, R., Mhlanga, M., Agou, F., Israël, A., and Laplantine, E. (2014). TNF and IL-1 exhibit distinct ubiquitin requirements for inducing NEMO-IKK supramolecular structures. J. Cell Biol. *204*, 231–245.

Ticau, S., Friedman, L.J., Champasa, K., Corrêa, I.R., Jr., Gelles, J., and Bell, S.P. (2017). Mechanism and timing of Mcm2-7 ring closure during DNA replication origin licensing. Nat. Struct. Mol. Biol. *24*, 309–315.

van Deursen, F., Sengupta, S., De Piccoli, G., Sanchez-Diaz, A., and Labib, K. (2012). Mcm10 associates with the loaded DNA helicase at replication origins and defines a novel step in its activation. EMBO J. *31*, 2195–2206.

van Mameren, J., Gross, P., Farge, G., Hooijman, P., Modesti, M., Falkenberg, M., Wuite, G.J., and Peterman, E.J. (2009). Unraveling the structure of DNA during overstretching by using multicolor, single-molecule fluorescence imaging. Proc. Natl. Acad. Sci. USA *106*, 18231–18236.

Warren, E.M., Vaithiyalingam, S., Haworth, J., Greer, B., Bielinsky, A.K., Chazin, W.J., and Eichman, B.F. (2008). Structural basis for DNA binding by replication initiator Mcm10. Structure *16*, 1892–1901.

Watase, G., Takisawa, H., and Kanemaki, M.T. (2012). Mcm10 plays a role in functioning of the eukaryotic replicative DNA helicase, Cdc45-Mcm-GINS. Curr. Biol. *22*, 343–349.

Worthington, A.S., and Burkart, M.D. (2006). One-pot chemo-enzymatic synthesis of reporter-modified proteins. Org. Biomol. Chem. *4*, 44–46.

Wu, R.A., Semlow, D.R., Kamimae-Lanning, A.N., Kochenova, O.V., Chistol, G., Hodskinson, M.R., Amunugama, R., Sparks, J.L., Wang, M., Deng, L., et al. (2019). TRAIP is a master regulator of DNA interstrand crosslink repair. Nature *567*, 267–272.

Wuite, G.J., Smith, S.B., Young, M., Keller, D., and Bustamante, C. (2000). Single-molecule studies of the effect of template tension on T7 DNA polymerase activity. Nature *404*, 103–106.

Yin, J., Lin, A.J., Golan, D.E., and Walsh, C.T. (2006). Site-specific protein labeling by Sfp phosphopantetheinyl transferase. Nat. Protoc. *1*, 280–285.

Yuan, Z., Bai, L., Sun, J., Georgescu, R., Liu, J., O'Donnell, M.E., and Li, H. (2016). Structure of the eukaryotic replicative CMG helicase suggests a pumpjack motion for translocation. Nat. Struct. Mol. Biol. *23*, 217–224.

Zhai, Y., Cheng, E., Wu, H., Li, N., Yung, P.Y., Gao, N., and Tye, B.K. (2017). Open-ringed structure of the Cdt1-Mcm2-7 complex as a precursor of the MCM double hexamer. Nat. Struct. Mol. Biol. *24*, 300–308.

Zhang, G.C., Kong, I.I., Kim, H., Liu, J.J., Cate, J.H., and Jin, Y.S. (2014). Construction of a quadruple auxotrophic mutant of an industrial polyploid saccharomyces cerevisiae strain by using RNA-guided Cas9 nuclease. Appl. Environ. Microbiol. *80*, 7694–7701.

Zhou, Z., Cironi, P., Lin, A.J., Xu, Y., Hrvatin, S., Golan, D.E., Silver, P.A., Walsh, C.T., and Yin, J. (2007). Genetically encoded short peptide tags for orthogonal protein labeling by Sfp and AcpS phosphopantetheinyl transferases. ACS Chem. Biol. *2*, 337–346.

STAR★METHODS

KEY RESOURCES TABLE

REAGENT or RESOURCE	SOURCE	IDENTIFIER
Antibodies		
Anti-digoxigenin, Fab fragments	Roche	Cat# 11 214 667 001; RRID: AB_514494
Bacterial and Virus Strains		
Escherichia coli BL21-DE3 codon plus RIL	Agilent	Cat# 230245
Escherichia coli BL21-DE3	Agilent	Cat# 200131
Escherichia coli Rosetta (DE3)	Novagen	Cat# 70954
Escherichia coli BLR(DE3)	Novagen	Cat# 69053
Chemicals, Peptides, and Recombinant Proteins		
Alexa Fluor 488 NHS Ester	ThermoFisher	Cat# A20000
Cy3 maleimide mono-reactive dye	GE Healthcare	Cat# PA23031
Cy5 NHS ester mono-reactive dye	GE Healthcare	Cat# PA15101
LD650 maleimide mono-reactive dye	Lumidyne Technologies	Cat# LD650-MAL
SYTOX Orange	ThermoFisher	Cat# S34861
DBCO-Cy5	Sigma-Aldrich	Cat# 777374
Coenzyme A trilithium salt	Sigma-Aldrich	Cat# C3019
Trolox	Sigma-Aldrich	Cat# 238813
4-Nitrobenzyl alcohol (NBA)	Sigma-Aldrich	Cat# N12821
Cyclooctatetraene (COT)	Sigma-Aldrich	Cat# 138924
Protocatechuate 3,4-Dioxygenase from *Pseudomonas* sp. (PCD)	Sigma-Aldrich	Cat# P8279
3,4-Dihydroxybenzoic acid (PCA)	Sigma-Aldrich	Cat# 37580
Streptavidin Coated Polystyrene Particles (4.0-4.9 μm)	Spherotech	Cat# SVP-40-5
M13mp18 Single-stranded DNA	New England BioLabs	Cat# N4040
^{32}P-α-dCTP	Perkin Elmer	Cat# BLU013H
DNA, lambda	Roche	Cat# 10745782001
Single-Stranded λ-DNA	LUMICKS	Cat# ss λ-DNA
Klenow Fragment	New England BioLabs	Cat# M0212
Biotin-11-dUTP Solution	ThermoFisher	Cat# R0081
Biotin-14-dCTP	ThermoFisher	Cat# 19518018
Digoxigenin-11-dUTP	Roche	Cat # 11558706910
5-azidomethyl-dUTP	Jena Bioscience	Cat # CLK-084
dNTP Set	ThermoFisher	Cat# 10297018
ATP solution	ThermoFisher	Cat# R0441
NTP Set	ThermoFisher	Cat# R0481
DNase I	New England BioLabs	Cat# M0303
3 x Flag-tag	EZBiolab	Cat# cp7204
Creatine Phosphokinase from rabbit muscle	Sigma-Aldrich	Cat# C3755
Phosphocreatine di(tris) salt	Sigma-Aldrich	Cat# P1937
PMSF Protease Inhibitor	ThermoFisher	Cat# 36978
DNase I	New England BioLabs	Cat# M0303
ANTI-FLAG M2 Affinity Gel	Sigma-Aldrich	Cat# A2220
Ni-NTA Agarose	QIAGEN	Cat# 30210
IPTG	Gold Biotechnology	Cat# I2481
Ampicillin sodium salt	Sigma-Aldrich	Cat# A0166

(*Continued on next page*)

Continued

REAGENT or RESOURCE	SOURCE	IDENTIFIER
Chloramphenicol	Sigma-Aldrich	Cat# C0378
Kanamycin sulfate from *Streptomyces kanamyceticus*	Sigma-Aldrich	Cat# K1377
Rapamycin	Sigma-Aldrich	Cat# R0395
Pol ε	Georgescu et al., 2014	N/A
Pol α-primase	Georgescu et al., 2015	N/A
RPA	Henricksen et al., 1994	N/A
RFC	Finkelstein et al., 2003	N/A
PCNA	Bauer and Burgers, 1988	N/A
CMG	Georgescu et al., 2014	N/A
CMG-S6	This paper	N/A
MTC complex	Langston et al., 2017	N/A
Mcm10	Langston et al., 2017	N/A
Mcm10-S6	This paper	N/A
Mcm10-ΔN	This paper	N/A
Mcm10-ΔC	This paper	N/A
SFP Synthase	Yin et al., 2006	N/A
Experimental Models: Organisms/Strains		
Saccharomyces cerevisiae strain W303	Brian Chait Lab (Rockefeller University)	N/A
Oligonucleotides		
See Table S1	IDT	N/A
Recombinant DNA		
pRSFDuet-1-Pol12 (Pol α-primase purification)	Georgescu et al., 2015	N/A
pCDFDuet-1-Pri1 (Pol α-primase purification)	Georgescu et al., 2015	N/A
pACYCDuet-1-Pri2 (Pol α-primase purification)	Georgescu et al., 2015	N/A
Pol 2-prs425/gal, with pJL6 (Pol ε purification)	Georgescu et al., 2014	N/A
JF.RPA.2.2 (RPA purification)	Georgescu et al., 2014	N/A
DZ.PCNA (PCNA purification)	Georgescu et al., 2014	N/A
JF.mcm10.0HCF (Mcm10 and Mcm10-ΔC purification)	Langston et al., 2017	N/A
JF.mcm10.0HS6CF (Mcm10-S6 purification)	This paper	N/A
JF.mcm10.delta1-128.0CF (Mcm10-ΔN purification)	This paper	N/A
pLANT-2/RIL-RFC[1+5] (RFC purification)	Finkelstein et al., 2003	N/A
pET(11a)-RFC[2+3+4] (RFC purification)	Finkelstein et al., 2003	N/A
Sfp pet29b C-terminal His Tag	Worthington and Burkart, 2006	Addgene Plasmid# 75015
Cas9-NAT	Zhang et al., 2014	Addgene Plasmid# 64329
gRNA-ura-HYB	Zhang et al., 2014	Addgene Plasmid# 64330
Software and Algorithms		
Origin vE9.5	OriginLab	https://www.originlab.com
MATLAB v2016b	MathWorks	https://www.mathworks.com/products/matlab.html
FIJI	Schindelin et al., 2012	https://imagej.net/Fiji
KymographDirect and KymographClear	Mangeol et al., 2016	https://sites.google.com/site/kymographanalysis/
@msdanalyzer MATLAB class	Tarantino et al., 2014	https://github.com/tinevez/msdanalyzer
MSD analysis MATLAB code	This paper	https://data.mendeley.com/datasets/vj3c828cxs
Instantaneous velocity analysis MATLAB code	This paper	https://data.mendeley.com/datasets/y7f6jbt6v7

LEAD CONTACT AND MATERIALS AVAILABILITY

Further information and requests for resources and reagents should be directed to and will be fulfilled by the Lead Contact, Shixin Liu (shixinliu@rockefeller.edu).

EXPERIMENTAL MODEL AND SUBJECT DETAILS

A W303 *Saccharomyces cerevisiae* strain (*ade2-1 ura3-1 his3-11,15 trp1-1 leu2-3,112 can1-100 bar1Δ MATa pep4::KANMX6*), a gift from the Brian Chait lab (Rockefeller University), was modified to express the proteins listed in the Key Resources Table using linearized plasmids with standard genetic procedures. Proteins purified from *E. coli* were transformed with plasmids for protein overexpression as listed in the Key Resources Table, and were overexpressed and purified as detailed below.

METHOD DETAILS

Protein purification and labeling

Replication-related proteins

With the exception of the Mcm10 truncation mutants, all unlabeled proteins used for *in vitro* reconstituted replication were purified as previously published: Pol ε and CMG (Georgescu et al., 2014), RFC (Finkelstein et al., 2003), PCNA (Bauer and Burgers, 1988), RPA (Henricksen et al., 1994), Pol α-primase (Georgescu et al., 2015), and Mcm10 and Mrc1-Tof1-Csm3 complex (Langston et al., 2017).

Pol ε

The four subunit Pol ε, containing a FLAG tag on the N terminus of Pol2, was transformed into yeast on the pRS425/GAL plasmid along with pJL6, expressing genes encoding Dpb2, Dpb3 and Dpb4. Expression was induced by galactose and Pol ε was subsequently purified using anti-FLAG agarose followed by a heparin Sepharose column (GE Healthcare). All buffers were degassed before use to prevent oxidation of any possible Fe-S centers. Pure protein was aliquoted, flash frozen and stored at −80°C.

Pol α-primase

Yeast expressing an integrated N-3XFLAG Pol 1 gene under control of the Gal1/10 promotor was grown/expressed. The Pol12, Pri1, and Pri2 subunits were cloned into *E. coli* vectors pRSFDuet-1, pCDFDuet-1, and pACYCDuet-1, respectively (Novagen). Pol12 and Pri1/Pri2 were separately transformed into *E. coli* BL21-DE3 codon plus RIL cells, then induced with IPTG for 8 h at 15°C. A 12 L culture of induced yeast cells for Pol1 and 1 L of each induced *E. coli* cultures for Pol12 and Pri1 and Pri2 were co-crushed in a cryogenic mill and Pol α-holoenzyme was purified on an anti-FLAG and then Mono S. All buffers were degassed before use to prevent oxidation of the Fe-S center. Pure protein was aliquoted, flash frozen and stored at −80°C.

RPA

Plasmids encoding RFA1, RFA2, RFA3 under control of the IPTG inducible promotor were transformed into *E. coli* BL21-DE3 cells and induced with IPTG for 16 h at 15°C. Protein was released from cells by French Press then clarified by centrifugation and loaded and on an Affi-Gel Blue column, and washed with 0.8 M KCl and 1.5 M NaSCN, desalted using a hydroxyapatite column in 80 mM potassium phosphate and then was further purified on a MonoQ column in 200 mM KCl and eluted with a gradient to 1M KCl. Pure protein was aliquoted, flash frozen and stored at −80°C.

RFC

No tags were used in this purification of WT *S. cerevisiae* RFC. pLANT-2/RIL–RFC[1+5] was co-transformed with pET(11a)-RFC [2+3+4] into BLR(DE3) cells (Novagen). The proteins were overexpressed in *E. coli* upon addition of IPTG for 8 h at 15°C overnight. Chromatography over a SP-Sepharose and then a Q-Sepharose column gave 95% pure protein, which was aliquoted, flash frozen and stored at −80°C.

PCNA

BL21 (DE3) *E. coli* cells were transformed with a T7 inducible plasmid encoding tagless PCNA, lysed using a French Press, and spun. The supernatant was treated with 150 mM ammonium sulfate and then 10% polyamine P, then spun again. 0.23 mg ammonium sulfate was added to the supernatant, and after centrifugation the supernatant was applied to MonoQ and then S-Sepharose to obtain > 95% pure protein. PCNA was then aliquoted, flash frozen and stored at −80°C.

CMG

CMG with a 3 × FLAG on Cdc45 and His tag on Mcm5, was purified by successive FLAG chromatography followed by nickel chelate chromatography, followed by gel filtration through a Superose 6 column in 25 mM Tris-OAc, pH 7.6, 40 mM KOAc, 40 mM K glutamate, 2 mM $Mg(OAc)_2$, 1 mM DTT, 20% glycerol and 0.25 mM EDTA. Pure CMG was aliquoted, flash frozen and stored at −80°C.

MTC complex

C-terminal Mrc1 3 × FLAG and Tof1, Csm3 were coexpressed under control of Gal1/10 and purified on a FLAG column and then injected onto a 24 mL Supersose 6 gel filtration column equilibrated in 20 mM Tris-Cl pH 7.5, 10% glycerol, 500 mM NaCl, 1 mM DTT, 1 mM $MgCl_2$, 0.01% NP-40. Pure protein was aliquoted, flash frozen and stored at −80°C.

Mcm10

S. cerevisiae Mcm10 containing a N-terminal His_6 tag and a C-terminal 3 × FLAG tag was expressed in *E. coli* BL21-DE3 codon plus RIL cells, then clarified extract was applied to Nickel-NTA agarose (GE Healthcare) and after elution, was applied to an anti-FLAG

agarose column (Sigma). Bound material was eluted with buffer containing 0.2 mg/mL 3 × FLAG peptide. Pure protein was aliquoted, flash frozen and stored at −80°C.

Mcm10-ΔN

To obtain Mcm10 missing the first 128 residues (Mcm10-ΔN; Figure S5B), *S. cerevisiae* Mcm10 (AA 129-571) bearing a 3 × FLAG tag at the C terminus was overexpressed in *E. coli* BL21-DE3 codon plus RIL cells in the presence of 0.1 mg/mL ampicillin. 6 L of cells were grown to an OD_{600} of 0.6 and induced with 0.8 mM IPTG for 16 h at 15°C. The cells were lysed by French press and clarified by centrifugation at 50,000 × g in the presence of 2 U/mL DNase I (New England BioLabs) and 1 mM PMSF for 30 min. Lysate was applied to 2 mL of anti-FLAG M2 agarose (Sigma-Aldrich) pre-equilibrated with buffer A (250 mM potassium glutamate, 50 mM HEPES pH 7.5, and 10% glycerol) by batch binding on a rocking shaker for 1 h at 4°C. The bound material was washed with 60 × column volume (CV) of buffer A followed by elution with 5 mL of buffer A containing 0.2 mg/mL 3 × FLAG peptide (EZ Biolab)—pausing 30 min every CV. Peak fractions were aliquoted, flash frozen, and stored at −80°C.

Mcm10-ΔC

To obtain Mcm10 missing residues 370-571 (Mcm10-ΔC; Figure S5B), *S. cerevisiae* Mcm10 bearing a 6 × His tag at the N terminus was overexpressed in *E. coli* BL21-DE3 codon plus RIL cells under ampicillin selection. 12 L of cells were grown to an OD_{600} of 0.6 and induced with 0.8 mM IPTG for 16 h at 15°C. The cells were lysed by French press and clarified by centrifugation at 50,000 × g in the presence of 2 U/mL DNase I (New England BioLabs) and 1 mM PMSF for 30 min. Lysate was applied to a 1 mL Ni-NTA Sepharose column (GE Healthcare) pre-equilibrated with buffer A (350 mM NaCl, 30 mM Tris-OAc pH 7.5, 5 mM imidazole, and 10% glycerol). The bound material was washed with a 30 × CV of buffer A followed by elution with a linear 15-700 mM imidazole gradient in buffer A. Mcm10 eluted between 180 and 350 mM imidazole. Peak fractions were pooled and dialyzed against 1 L of 100 mM NaCl, 30 mM Tris-OAc pH 7.5, and 10% glycerol overnight at 4°C. Mcm10 was subsequently loaded onto a 1 mL sulphopropyl cation exchange column (GE healthcare) and eluted with a 200-800 mM NaCl gradient in 10% glycerol, 30 mM HEPES pH 7.5, and 0.05% Tween 20. Full-length Mcm10 eluted between 400 and 500 mM NaCl, whereas a C-terminal truncation product eluted around 250 mM NaCl. The Mcm10 cleavage product was confirmed by mass spectrometry to be residues 1-369. Peak fractions were pooled, diluted to a conductivity equal to 250 mM NaCl with 10% glycerol, 30 mM HEPES pH 7.5, 4 mM DTT, and 40 μg/mL BSA, aliquoted, flash frozen, and stored at −80°C.

SFP synthase reagents for protein labeling

Site-specific labeling of CMG and Mcm10 used SFP synthase (4'-phosphopantetheinyl transferase), which specifically recognizes a short peptide tag and catalyzes the covalent transfer of CoA-functionalized moieties to a single serine residue within the tag via a phosphopantetheinyl linker. Sfp pet29b C-terminal His Tag was a gift from Michael Burkart (Addgene #75015) (Worthington and Burkart, 2006). SFP synthase was overexpressed in *E. coli* BL21-DE3 and purified on a nickel-NTA column as previously described (Yin et al., 2006), with minor modifications. 3 L of cells were grown in LB medium in the presence of 50 μg/mL kanamycin to an OD_{600} of 0.5 and induced with 0.5 mM IPTG for 4 h at 37°C. Cell pellets were resuspended in cold lysis buffer (20 mM Tris HCl pH 7.9, 500 mM NaCl, 5 mM imidazole pH 8.0) and then lysed by sonication on ice. Lysate was applied by gravity flow to 2 mL Ni-NTA agarose pre-equilibrated in lysis buffer. The bound material was washed with 4 × CV of lysis buffer, followed by 0.25 mL stepwise elution (20 mM Tris HCl pH 7.9, 500 mM NaCl, 250 mM imidazole pH 8.0). Peak fractions were pooled, analyzed by SDS-PAGE, dialyzed at 4°C into 50 mM HEPES pH 7.4, 150 mM NaCl, 50% glycerol, and stored at −20°C.

Cy3 and LD650 [a photostable version of Cy5 (Altman et al., 2011); Lumidyne Technologies] were functionalized by CoA and purified by HPLC as previously described (Yin et al., 2006), with minor modifications. 400 nmol LD650-maleimide was resuspended to 20 mM in DMSO and mixed with a ten-fold molar excess of Coenzyme A trilithium salt in 100 mM sodium phosphate pH 7.0 in a total volume 400 μL. The reaction was incubated for 1.5 h at room temperature, and subsequently quenched with an excess of 2-Mercaptoethanol. LD650-CoA was separated from excess CoA and unreacted dye by reverse phase chromatography (Agilent Pursuit XRS C18). Sample was loaded in Buffer A (10 mM triethylamine acetate pH 7.0) and eluted with a gradient into Buffer B (10 mM triethylamine acetate pH 7.0; 50% acetonitrile). LD650-CoA eluted at ~70% Buffer B, prior to free dye and after excess CoA. Acetonitrile was removed by SpeedVac, and the sample was desalted and eluted in methanol using a Sep-Pak C18 cartridge (Waters). Samples were then aliquoted, dried by SpeedVac, and stored at −80°C.

Cy3-CMG

To obtain CMG labeled with a single Cy3, we inserted the "S6" peptide (GDSLSWLLRLLN) (Zhou et al., 2007) between the C terminus of Cdc45 and its 3 × FLAG tag. To insert the S6 sequence, we transformed and co-expressed Cas9, gRNA targeting a region downstream of the Cdc45 C terminus, and a ssDNA encoding the S6 peptide into the CMG co-expression strain. Nourseothricin-resistant Cas9-NAT (Addgene #64329) and hygromycin-resistant gRNA-ura-HYB (Addgene #64330) plasmids were gifts from Yong-Su Jin (Zhang et al., 2014). The gRNA sequence of the gRNA-ura-HYB plasmid was mutated with the Q5 mutagenesis kit (New England BioLabs) to ACTAGTTAACAATCCACTCA in order to hybridize with a 20-nt region downstream of Cdc45. The DNA donor (ACGGACACTTACTTGGTTGCTGGGTTAACACCTAGGTATCCTCGCGGACTAGACACGATACACACAAAAAAACC TATTTTGAATAATTTCAGCATGGCGTTTCAACAAATAACTGCAGAAACGGATGCTAAAGTGAGAATAGATAATTTTGAAAGTTCCATA ATTGAAATACGTCGTGAAGATCTTTCACCATTCCTGGAGAAGCTGACCTTGAGTGGATTGTTAGGATCTGGCGATAGCCTGAGCT GGCTGCTGCGCCTGCTGAACACTAGTGACTACAAAGACCATGACGGTGATTATAAAGATCATGACATCGACTACAAGGATGACGAT GACAAGTAGGGATCCGGCTGCTAACAAAGCCCGAAAGGAAGCTGAGTTGGCTGCTGCCACCGCTGAGCGGCCGCCAGGTGGAT GGGGGTAATATAATTGTATCTATGTATCTGG) was purchased from IDT. The underlined sequence encodes the S6 peptide.

Co-transformants of these constructs were grown under auxotrophic (–Ade –His –Leu –Trp –Ura) and antibiotic (hygromycin and nourseothricin) selection in SC glucose, streaked on selective plates, and colonies were sequenced to confirm the existence of the S6 tag. The resultant CMG-S6 construct was overexpressed and purified as previously described (Georgescu et al., 2014). CMG-S6, SFP, and Cy3-CoA were then incubated at a 1:2:5 molar ratio for 1 h at room temperature in the presence of 10 mM $MgCl_2$. Excess dye and SFP were removed by purification on a Sepharose 6 column (GE Healthcare) with a buffer containing 150 mM NaCl, 10% glycerol, 20 mM Tris-HCl pH 7.5, 1 mM $MgCl_2$, and 1 mM DTT. The final labeling ratio was estimated to be ~100% from the extinction coefficients of Cy3 and CMG (Figure S1A). Peak fractions were aliquoted, flash frozen, and stored at −80°C.

LD650-Mcm10

To obtain Mcm10 labeled with a single LD650, we overexpressed *S. cerevisiae* Mcm10 bearing a hexahistidine tag followed by the S6 peptide at the N terminus and a 3 × FLAG tag at the C terminus in *Escherichia coli* BL21-DE3 codon plus RIL cells under ampicillin and chloramphenicol selection. 12 L of cells were grown to an OD_{600} of 0.6 and induced with 0.8 mM IPTG for 4 h at 20°C. The cells were lysed by French press and clarified by centrifugation at 50,000 × g in the presence of 2 U/mL DNase I (New England BioLabs) and 1 mM PMSF for 30 min. Lysate was applied to a column packed with 4 mL of anti-FLAG M2 agarose (Sigma-Aldrich) pre-equilibrated with buffer A (750 mM NaCl, 100 mM potassium glutamate, 30 mM Tris-OAc pH 7.9, 15 mM imidazole, and 10% glycerol). The bound material was washed with a 20 × column volume (CV) of buffer A followed by elution with 25 mL of buffer A containing 0.2 mg/mL 3 × FLAG peptide (EZ Biolab)—pausing 30 min every CV—directly onto a 1-mL Ni-NTA column (GE Healthcare). The Ni-NTA column was subsequently washed with 20 × CV buffer A and eluted with a linear 15-700 mM imidazole gradient in buffer A. Mcm10-S6 eluted between 180 and 350 mM imidazole. Peak fractions were pooled and dialyzed against 1 L of 300 mM NaCl, 30 mM Tris-OAc pH 8.0, and 10% glycerol overnight at 4°C. Mcm10 was subsequently labeled with LD650 at the N terminus by incubating Mcm10-S6, SFP, and LD650-CoA at a 1:2:3 molar ratio for 1 h at room temperature. To remove free dye and SFP, Mcm10-LD650 was diluted with 10% glycerol and 30 mM Tris-OAc pH 8.0 to reach a conductivity equal to 200 mM NaCl, loaded onto a column packed with 1 mL of sulphopropyl cation exchange resin (GE healthcare) and eluted with a 200-800 mM NaCl gradient in 10% glycerol, 30 mM HEPES pH 7.5, and 0.05% Tween 20. LD650-Mcm10 was eluted between 400 and 500 mM NaCl. The final labeling ratio was estimated to be ~100% from the extinction coefficients of LD650 and Mcm10 (Figure S1B). Peak fractions were pooled, diluted to a conductivity equal to 250 mM NaCl with 10% glycerol, 30 mM HEPES pH 7.5, 4 mM DTT, and 40 μg/mL BSA, aliquoted, flash frozen, and stored at −80°C.

A488-RPA

S. cerevisiae RPA heterotrimer was purified as previously described (Henricksen et al., 1994). We used Alexa Fluor 488 (A488) NHS ester (Thermo Fisher) to nonspecifically label the primary amines of RPA. Preferential N-terminal labeling was achieved by labeling at low pH (7.0) for an NHS ester reaction (Sélo et al., 1996). Labeling was performed with 50 mM HEPES pH 7.0, 150 mM NaCl, 1 mM DTT, and 0.25 mM EDTA. RPA was incubated with A488 dye at a 1:5 molar ratio for 1 h at room temperature, and the reaction was quenched with 25 mM Tris-HCl pH 6.8 for 5 min. Excess dye was removed from RPA by buffer exchange with 20% glycerol, 30 mM HEPES pH 7.9, 150 mM NaCl, 1 mM DTT, and 0.25 mM EDTA. The final labeling ratio was estimated to be ~90% from the extinction coefficients of A488 and RPA heterotrimer (Figure S1C). The final A488-RPA complex was aliquoted and stored at −80°C.

Cy5-anti-Dig

Anti-digoxigenin antigen-binding fragments (Fab; Roche) were resuspended in 0.1 M $NaHCO_3$ pH 8.3 at 10 mg/mL. Cy5-NHS ester (GE Healthcare) was resuspended in DMSO. Dye was incubated with Fab at a 4:1 molar ratio for 1 h at room temperature. The reaction was quenched with 25 mM Tris-HCl pH 6.8 for 5 min. Free dye was removed by a P-30 gel spin column (BioRad). The final labeling ratio was estimated to be 2.8:1. Cy5-anti-Dig was aliquoted, flash frozen, and stored at −80°C.

Cy3-CMG containing a rapamycin-inducible Mcm2-Mcm5 linkage

To obtain Cy3-CMG with an inducible Mcm2-Mcm5 linkage, we used CRISPR-Cas9 genome editing as above to modify CMG-Cdc45-S6; the FKBP-rapamycin binding (FRB) and FK506-binding protein (FKBP) domains were inserted into Mcm2 and Mcm5, respectively (Figures S6A and S6B). In the presence of rapamycin, these domains form an inducible linkage that closes the Mcm2/5 gate (Samel et al., 2014). To generate this strain, the FRB domain with linkers (AIAGANTCTPRGSGMLPSGMASRILWHEMWHEGLEEASRLYFGERNVKGMFEVLEPLHAMMERGPQTLKETSFNQAYGRDLMEAQEWCRKYMKSGNVKDLTQAWDLYYHVFRRISKTSYPYDVPDYAGANDGAAIA) was first inserted into Mcm2 at AA 221 using the protocol and Cas9-NAT/gRNA-ura-HYB plasmids described above, in which the gRNA was mutated to GCTGGAATATACAGATGAAA to target near the desired insertion site. The codon-optimized donor (Mcm2-FRB DNA donor) was purchased from IDT and its sequence can be found in Table S1. Note that the insertion site spanned the PAM, obviating the need to silently mutate the donor DNA in the gRNA targeting region.

Following transformant selection, sequencing, and passive gRNA plasmid curing, the resulting CMG-Cdc45-S6-Mcm2-FRB strain was similarly edited to contain Mcm5-FKBP. The FKBP domain with linkers (SSYPYDVPDYASLGGPSSPKKKRKVSRGVQVETISPGDGRTFPKRGQTCVVHYTGMLEDGKKFDSSRDRNKPFKFMLGKQEVIRGWEEGVAQMSVGQRAKLTISPDYAYGATGHPGIIPPHATLVFDVELLKLETSYISFLNSDLINSRTQRVDGQIGAP) was inserted at AA 72 using the Cas9-NAT and gRNA-ura-HYB plasmids, in which the gRNA was mutated to GTTAACATGGAGCATTTGAT to target near the desired insertion site. The codon-optimized donor (Mcm5-FKBP DNA donor) was purchased from IDT and its sequence can be found in Table S1. To prevent gRNA targeting of the edited genome, three silent mutations were placed in the gRNA-targeting region of the donor DNA. Note that both the endogenous and overexpressed copies of Mcm2/5 were mutated to contain the FRB/FKBP domains, respectively. Following transformant

selection and sequencing, the resulting CMG-Cdc45-S6-Mcm2-FRB-Mcm5-FKBP construct was overexpressed, purified, and site-specifically labeled with Cy3 as described above.

DNA Substrate Preparation

Biotinylated dsDNA

To create a terminally biotinylated double-stranded DNA template, the 12-base 5′ overhang on each end of genomic DNA from bacteriophage λ (48,502 bp; Roche) was filled in with a mixture of natural and biotinylated nucleotides by the exonuclease-deficient DNA polymerase I Klenow fragment (New England BioLabs). Reaction was conducted by incubating 10 nM λ-DNA, 33 μM each of dGTP/dATP/biotin-11-dUTP/biotin-14-dCTP (Thermo Fisher), and 5 U Klenow in 1 × NEB2 buffer at 37°C for 45 min, followed by heat inactivation for 20 min at 75°C. DNA was then ethanol precipitated overnight at −20°C in 2.5 × volume cold ethanol and 300 mM sodium acetate pH 5.2. Precipitated DNA was recovered by centrifugation at 20,000 × g for 15 min at 4°C. After removing the supernatant, the pellet was air-dried, resuspended in TE buffer (10 mM Tris-HCl pH 8.0, 1 mM EDTA) and stored at 4°C.

Biotinylated ssDNA

Double-stranded λ DNA with one strand containing 4 biotins each at its 5′ and 3′ ends was obtained from LUMICKS (Amsterdam, Netherlands). A single dsDNA molecule was first captured between two beads, as assessed by a characteristic force-extension (*F-x*) curve (Figures S2A and S2B) (Smith et al., 1996). The non-biotinylated strand was then removed by overstretching the dsDNA at 0.1 μm/s under a low flow of 10 mM Tris-HCl pH 8.0, based on a previously published protocol (Candelli et al., 2013). Establishment of a ssDNA tether was verified by its characteristic *F-x* curve (Figure S2B). Subsequently, tether polarity was assigned in an orthogonal channel by visualizing the annealing site of a 500-mer (Table S1) stained with 10nM SYTOX Orange in 10mM Tris-HCl pH 7.5, 20 mM $MgCl_2$, and 200 mM NaCl.

Bulk Helicase Unwinding Assay

Circular M13 bacteriophage ssDNA (6.4 kbp; New England BioLabs) was annealed to a 5′-^{32}P labeled oligo containing a 5′-dT_{60} flap and a 35-nt sequence at its 3′ end that is complementary to M13 (Figure 2C). 0.5 nM of this substrate was incubated with 20 nM CMG in the presence or absence of 40 nM Mcm10 for 2 min. Reactions were initiated with 1 mM ATP, followed by an addition of 20 μM unlabeled flap oligo 2 min after initiation to prevent unwound radiolabeled oligo from reannealing to the M13 substrate. Aliquots were stopped with a final concentration of 1% SDS and 20 mM EDTA and flash frozen in liquid nitrogen. All reactions took place at 30°C and in 5% glycerol, 40 mg/mL BSA, 5 mM TCEP, 10 mM magnesium sulfate, 25 mM KCl, 25 mM Tris acetate pH 7.5, and 0.1 mM EDTA. Flap displacement was resolved by 10% PAGE, exposed to a phosphorimager screen, and imaged with Typhoon 9500 (GE healthcare).

Bulk Replication Assay

Unprimed, nucleotide-biased 3.2-kb forked DNA substrates that lack dC on the leading strand and dG on the lagging strand were used such that incorporation of ^{32}P-α-dCTP reported on leading-strand replication only (Schauer et al., 2017). 1.5 nM of DNA substrate was incubated with 40 nM CMG and 60 nM Mcm10 in the presence or absence of 5 μM Dig-dUTP for 10 min at room temperature. Subsequently, 15 nM Pol α, 15 nM Pol ε, 30 nM MTC, 5 nM RFC, 25 nM PCNA, 20 μM dATP, and 20 μM dCTP was added and the reaction incubated for 2 min at room temperature. The reaction was initiated with 5 mM ATP, 20 μM dGTP, 20 μM dTTP, and 125 nCi/μL ^{32}P-α-dCTP, and aliquots were stopped with a final concentration of 1% SDS and 20 mM EDTA. Reactions were run on 1.2% (wt/vol) alkaline agarose gel for 17 h at 35 V, backed with DE81 paper, and dried by compression. The gel was exposed to a phosphorimager screen and imaged with Typhoon 9500. Reaction volumes were 20 μL and took place at room temperature and in 5% glycerol, 80 μg/mL BSA, 5 mM TCEP, 10 mM magnesium acetate, 50 mM potassium glutamate, 25 mM Tris acetate pH 7.5, and 0.1 mM EDTA.

Single-Molecule Experiments

Data acquisition

Single-molecule experiments were performed at room temperature on a LUMICKS C-Trap instrument combining three-color confocal fluorescence microscopy with dual-trap optical tweezers (Hashemi Shabestari et al., 2017). A computer-controlled stage enabled rapid movement of the optical traps within a five-channel flow cell (Figure 1A). Laminar flow separated channels 1-3, which were used to form DNA tethers between 4.35-μm streptavidin-coated polystyrene beads (Spherotech) held in traps with a stiffness of 0.3 pN/nm. Under constant flow, a single bead was caught in each trap in channel 1. The traps were then quickly moved to channel 2 containing the biotinylated DNA of interest. By moving one trap against the direction of flow but toward the other trap, and vice versa, a DNA tether could be formed and detected via a change in the *F-x* curve. The traps were then moved to channel 3 containing only buffer, and the presence of a single DNA was verified by the *F-x* curve. Orthogonal channels 4 and 5 served as protein loading and/or experimental imaging chambers as described for each assay. Unless otherwise noted, flow was turned off during data acquisition. Force data was collected at 50 kHz. A488, Cy3, and LD650 fluorophores were excited by three laser lines at 488 nm, 532 nm, and 638 nm, respectively. Kymographs were generated via a confocal line scan through the center of the two beads at 0.142 s/line (mode-switching data), 0.634 s/line (replication data), or 1.16 s/line (ssDNA data).

Visualization of CMG on ssDNA

To investigate the ability of Cy3-CMG to load and translocate on ssDNA, optical traps tethering a single-stranded biotin-λ DNA (Figure S2) under a constant 5 pN tension were moved into channel 4 of the microfluidic flow cell (Figure 1A) containing 5 nM Cy3-CMG ± 10 nM Mcm10 in the following buffer: 25 mM Tris acetate pH 7.5, 5% glycerol, 40 μg/mL BSA, 3 mM DTT, 2 mM TCEP, 0.1 mM EDTA, 10 mM magnesium acetate, 50 mM potassium glutamate, and 1 mM ATP. In addition, the imaging buffer was supplemented with a triplet-state quenching cocktail (Dave et al., 2009) of 1 mM cyclooctatetraene (Sigma), 1 mM 4-nitrobenzyl alcohol (Sigma) and 1 mM Trolox (Sigma), as well as an oxygen scavenging system (Aitken et al., 2008) containing 10 nM protocatechuate-3,4-dioxygenase (Sigma) and 2.5 mM protocatechuic acid (Sigma). Following CMG loading, the tether was dragged to channel 5 that contained imaging buffer ± 1 mM ATP, supplemented with an ATP-regeneration system containing 60 μg/mL creatine phosphokinase (Sigma) and 20 mM phosphocreatine (Sigma). To determine if a closed Mcm2/5 gate affects ssDNA loading, a similar protocol was performed as above in the absence or presence of 1 μM rapamycin. This assay was performed with a higher concentration of CMGM [25 nM Cy3-CMG(Mcm2/5) + 60 nM Mcm10], and only briefly incubated (< 5 s) in channel 4 to better highlight differences ± rapamycin.

Detection of in situ DNA replication

To test whether Cy3-CMG can restart replication, optical traps tethering a double-stranded biotin-λ DNA under low tension were moved into channel 4 containing 30 nM Cy3-CMG, 60 nM Mcm10, and 1mM ATP. CMGM loading was promoted by stretching the tether to ~65 pN (20 μm tether length, or ~1.2 times its contour length). The CMGM-loaded tether was then dragged to channel 5 containing 5 mM ATP, and the additional *S. cerevisiae* proteins required for *in vitro* replication, purified as previously described (Georgescu et al., 2014; Lewis et al., 2017): 15 nM Pol α-primase, 15 nM Pol ε, 20 nM of Mrc1-Tof1-Csm3 heterotrimer, 5 nM RFC, and 25 nM PCNA. The imaging buffer described above was supplemented with 20 μM each of dATP/dCTP/dGTP/dTTP, and 100 μM each of rUTP/rCTP/rGTP. Upon lowering the force by decreasing the tether length to 15.1 μm (~0.92 times its contour length) to promote strand reannealing and fork collapse, directed motion of Cy3-CMG was observed (Figure 4B).

To confirm that this activity was due to replication, a similar experiment was performed in which optical traps tethering a double-stranded biotin-λ DNA under low tension were moved into channel 4 containing 30 nM Cy3-CMG, 60 nM Mcm10, 2 nM A488-RPA, 5 mM ATP, the additional *S. cerevisiae* proteins required for *in vitro* replication detailed above, as well as 20 μM each of dATP/dCTP/dGTP/dTTP, 100 μM each of rUTP/rCTP/rGTP, and 5 μM digoxigenin-11-dUTP (Roche). The tether was stretched to ~65 pN in order to create single-stranded regions and promote replisome assembly at the fork, determined by visualization of Cy3-CMG and A488-RPA. Following replisome loading, the tether was held at a constant low force for 5 to 10 min. Replication was assessed by dragging the tether to channel 5 containing imaging buffer supplemented with 50 nM Cy5-anti-Dig Fab (Figure S3A). Bulk analysis of replication in the presence of Dig-dUTP revealed severe inhibition of replisome speed (Figure S3C), accounting for the lack of CMGM movement in the single-molecule Dig-dUTP replication experiments (Figures 4A and S3B). Single-molecule DNA replication was also detected *in situ* using a similar approach to the Dig-dUTP experiment (Figures S3D and S3E), except 2.5 μM 5-azidomethyl-dUTP was used in place of Dig-dUTP. Nascent DNA was subsequently stained using 250 nM DBCO-Cy5 via copper-free click chemistry (Eeftens et al., 2015).

Observation of CMG mode-switching

Optical traps tethering a double-stranded biotin-λ DNA under a constant 10 pN tension were moved into channel 4 containing 30 nM Cy3-CMG ± 60 nM Mcm10 in imaging buffer supplemented with 5 mM ATP. The tether was stretched to ~65 pN in order to create ssDNA regions and promote CMG loading at the fork. Following the visualization of CMG loading, the tension was lowered to a constant force of 10 pN. Repeated cycles of this sequential force protocol were conducted to increase throughput. This assay was also performed as two-color (2 nM A488-RPA + 30 nM Cy3-CMG; or 30 nM Cy3-CMG + 60 nM LD650-Mcm10) and three-color (2 nM A488-RPA + 30 nM Cy3-CMG + 60 nM LD650-Mcm10) experiments. The effect of a closed Mcm2/5 gate on mode-switching was performed in the presence of 1 μM rapamycin.

Data analysis

Single-molecule force and fluorescence data were analyzed using custom software provided by LUMICKS. The loading efficiency of CMG on ssDNA ± Mcm10 was determined per tether by dividing the number of CMG complexes stably bound to ssDNA by the incubation time (~5 min in the absence of Mcm10 and ~30 s in its presence) in the CMG channel (channel 4). Only stably bound CMG molecules were considered, defined as those that survived dragging from channel 4 to channel 5. 62 out of 92 bound CMGs (67%) displayed unidirectional translocation and did so at an approximately constant speed (Figure 1B), enabling rate calculation by dividing the distance traveled by the duration of each trajectory (end-point velocities). This approach was validated by also performing a previously described (Galburt et al., 2009) pausing analysis as follows: position versus time data was extracted from each trajectory as described in the mean-square-displacement methods below, and subsequently smoothed using a third-order Savitzky-Golay filter. Instantaneous velocities were then computed from the slope of adjacent smoothed time points. A histogram containing all instantaneous velocities was well fit by a single Gaussian (Figure S2F) – centered similarly to the end-point velocity mean – as expected for approximately constant, pause-free trajectories. The lack of a peak at zero indicates the lack of a significant pausing state. For the dsDNA template, the speed of directed motion of CMGM in the presence of replication components was similarly calculated (Figures 4B and 4C). Mode-switch probabilities were calculated from the mean of per tether analyses, normalized to the mean of the CMGM condition. Mean-square-displacement (MSD) analysis of CMG diffusion was performed as follows. Segments of kymographs containing diffusive CMGs were cropped in Fiji (Schindelin et al., 2012). The KymographClear Fiji plugin and the

standalone KymographDirect software (Mangeol et al., 2016) were used to extract position versus time information from each diffusing CMG trajectory. Distance was converted to base pairs using the force-extension characteristics of λ DNA. MSD calculations were performed in MATLAB using the @msdanalyzer class (https://github.com/tinevez/msdanalyzer) (Tarantino et al., 2014) with custom modifications. 35 out of 48 analyzed trajectories (73%) displayed a linear MSD profile for Δt from 0 to 25% of the length of the trajectory [$R^2 = 0.96 \pm 0.05$ (mean ± SD) for linear regression]. A diffusion coefficient was obtained for each CMG trajectory that fits this criterion (Figure 5D).

QUANTIFICATION AND STATISTICAL ANALYSIS

The number of molecules or events analyzed is indicated in the text or figure legends. Errors reported in this study represent the approximated standard error of the mean determined from 100,000 bootstrapped samples for each dataset. *P value*s were determined from two-tailed two-sample t tests (*$p < 0.05$; **$p < 0.01$; ***$p < 0.001$).

DATA AND CODE AVAILABILITY

Raw data are available upon reasonable request. Analysis codes have been deposited to Mendeley (https://data.mendeley.com/datasets/vj3c828cxs; and https://data.mendeley.com/datasets/y7f6jbt6v7).

Cell

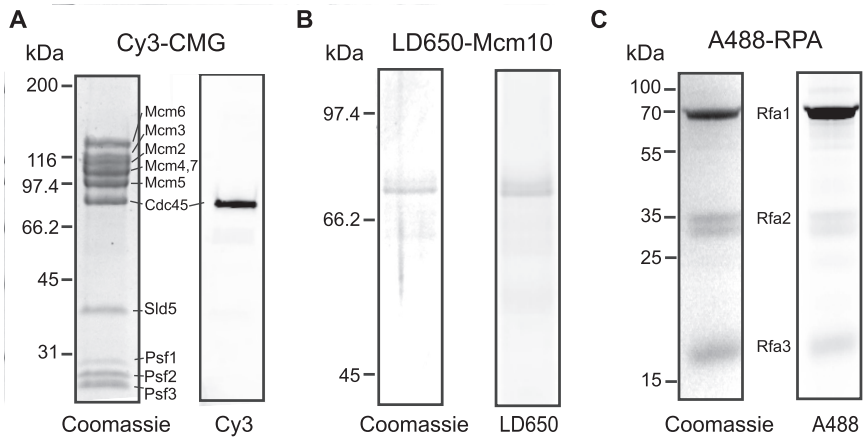

Figure S1. Protein Purification and Fluorescent Labeling, Related to Figures 1, 2, and 3

The purity of Cy3-CMG (A), LD650-Mcm10 (B), and A488-RPA (C) was analyzed by SDS-PAGE via Coomassie Blue staining (Left) and fluorescence scan (Right). See STAR Methods for detailed purification and labeling procedures.

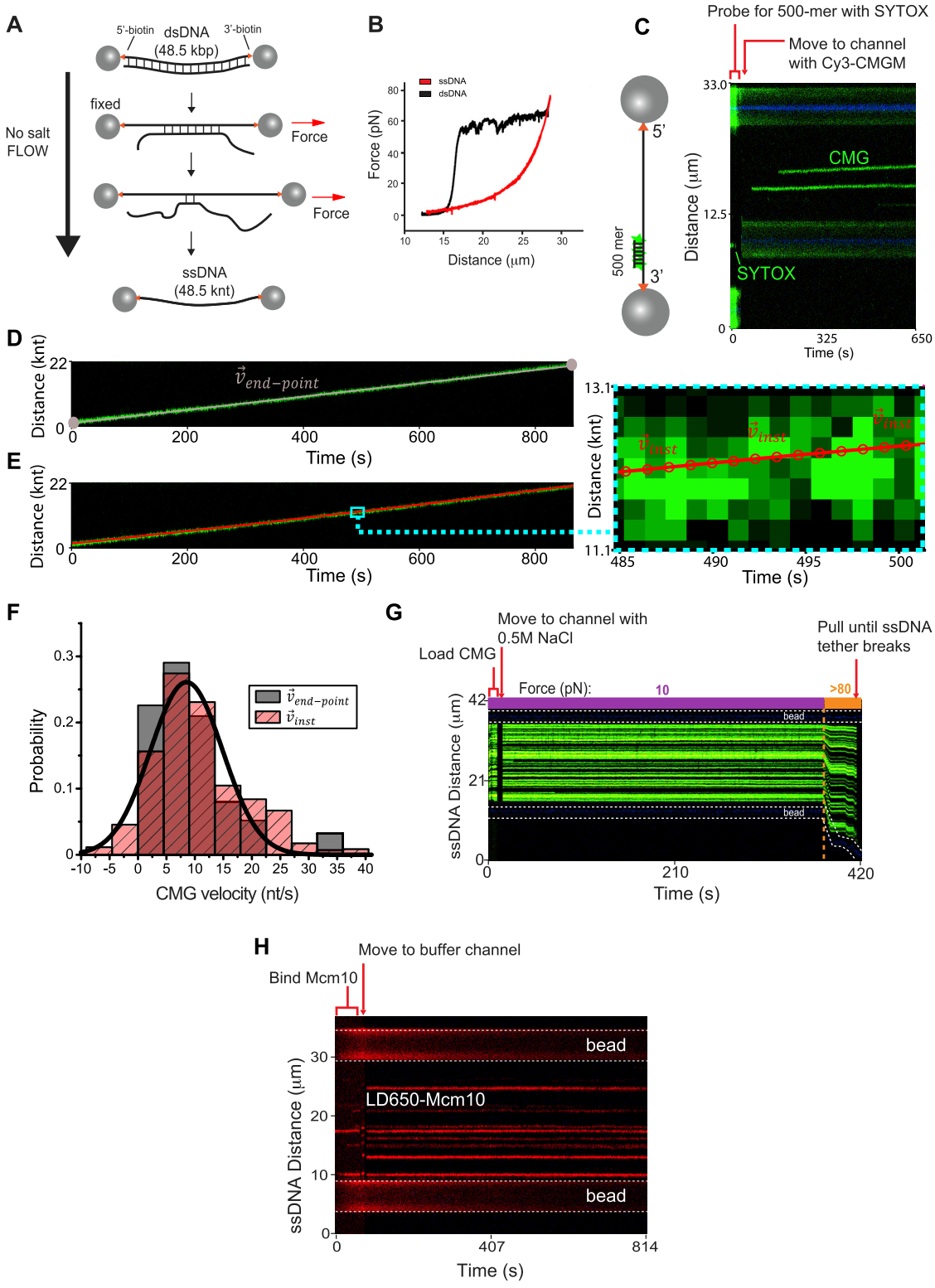

Figure S2. Additional Characterization of CMG and Mcm10 Behavior on ssDNA Tethers, Related to Figures 1 and 2

(A) Schematic illustrating *in situ* formation of a ssDNA tether. Two optically trapped streptavidin-coated beads were used to capture a single dsDNA biotinylated on both ends of one strand. The non-biotinylated strand was then removed by force-induced melting of the duplex, aided by low flow in a buffer lacking salt.
(B) Force-extension curve indicating the transition from dsDNA (black) to ssDNA (red).

(legend continued on next page)

(C) (left) Cartoon schematic illustrating ssDNA polarity assignment (not drawn to scale). (right) Representative kymograph of a CMG translocation polarity experiment, in which a 500-mer was annealed near the 3′ end of a ssDNA tether and visualized via SYTOX orange staining. Cy3-CMG translocation was subsequently observed in an orthogonal channel.

(D) A representative kymograph of CMG translocating on ssDNA is shown. A schematic is overlaid demonstrating the end-point velocity calculation ($\vec{v}_{end-point}$), in which the first and last position/time points are used to compute the velocity of each trajectory.

(E) The same kymograph as in (D), except that CMG's trajectory has been fit at each time frame. The inset shows that each pair of adjacent time points are used to calculate an instantaneous velocity ($\vec{v}_{inst}$), resulting in hundreds of velocities per trajectory.

(F) Distribution of CMG translocation rates on ssDNA as calculated by end-point (gray) or instantaneous (red) methods. A single Gaussian is fit to the distribution of instantaneous velocities, closely matching the end-point velocities. The lack of a bimodal instantaneous velocity distribution with a peak at zero suggests that pausing is rare.

(G) Shown is a kymograph in which Cy3-CMGM (green) was first loaded onto ssDNA at low salt (50 mM potassium glutamate) and low force (10 pN) in the absence of ATP. The tether was then dragged to a new channel containing high salt (0.5 M NaCl + 50 mM potassium glutamate) followed by an increase of force applied to the DNA to > 80 pN. In this example, the ssDNA tether was incubated with an elevated CMGM concentration compared to the experiments described in the main text (e.g., in Figure 1B) in order to overload the tether with CMGM. The ability of CMG to withstand hydrodynamic dragging, high salt and high tension in the tether collectively suggests that it encircles ssDNA.

(H) Representative kymograph demonstrating that LD650-Mcm10 (red) alone stably binds to ssDNA without CMG.

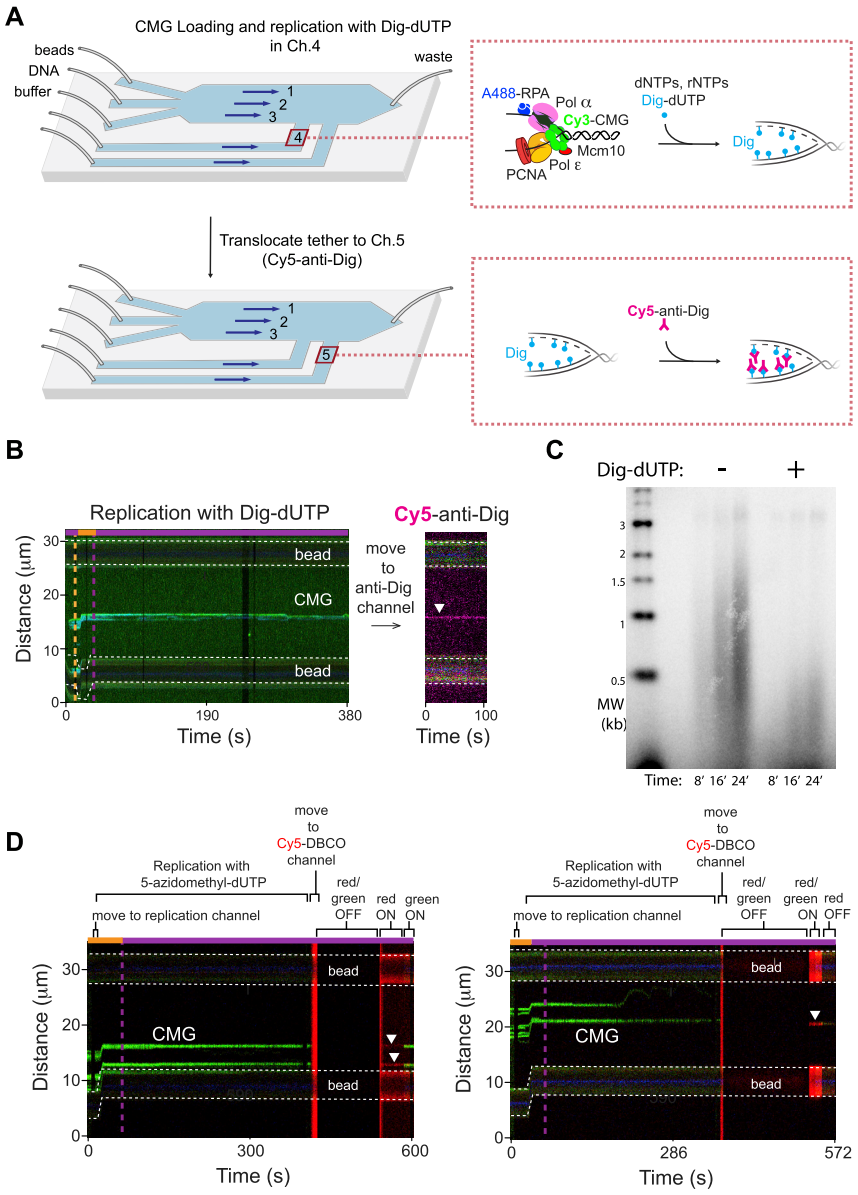

Figure S3. Visualization of DNA Replication with Modified Nucleotides, Related to Figure 4

(A) Schematic of the experimental setup for detection of Dig-dUTP incorporation. (Top) Cy3-CMGM and other unlabeled replisome components were loaded at a DNA fork initially marked by A488-RPA and incubated with a full set of nucleotides and Dig-dUTP. (Bottom) The post-replication assembly was moved to a separate channel containing Cy5-anti-Dig for staining nascent DNA.

(B) A representative kymograph of *in situ* DNA replication using Dig-dUTP. The nascent DNA tract (magenta) was observed at the same location as CMGM.

(C) Dig-dUTP inhibits replication. Replication of a 3.2-kb forked DNA substrate was stopped at the indicated time points (see STAR Methods).

(D) Representative kymographs of *in situ* DNA replication using 5-azidomethyl-dUTP. Cy3-CMGM and other unlabeled replisome components were loaded at a DNA fork and incubated with a full set of nucleotides including 5-azidomethyl-dUTP. Nascent DNA was subsequently stained with Cy5-DBCO in an orthogonal channel of the flow cell, and was observed at the same location as CMGM (indicated by arrows).

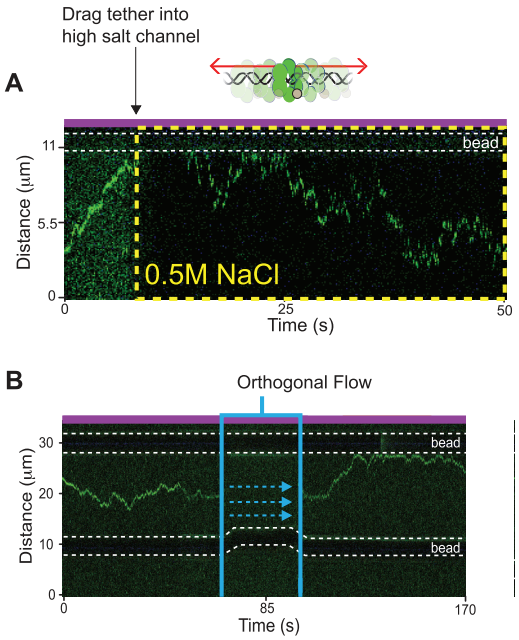

Figure S4. Additional Characterization of CMGM Diffusion on dsDNA, Related to Figure 5

(A) Following a CMGM mode-switch in low salt (e.g., as shown in Figure 5A), the tether bound with a diffusing CMGM was moved to a channel containing 0.5 M NaCl, but no free CMGM. CMGM persisted in the diffusive mode under high salt.

(B) Kymograph showing that CMGM, while in the diffusive mode, persists on dsDNA under hydrodynamic force generated by an orthogonal flow. The tether temporarily went out of the imaging plane when the flow was applied. Together, these results suggest that CMGM is topologically linked to dsDNA during diffusion.

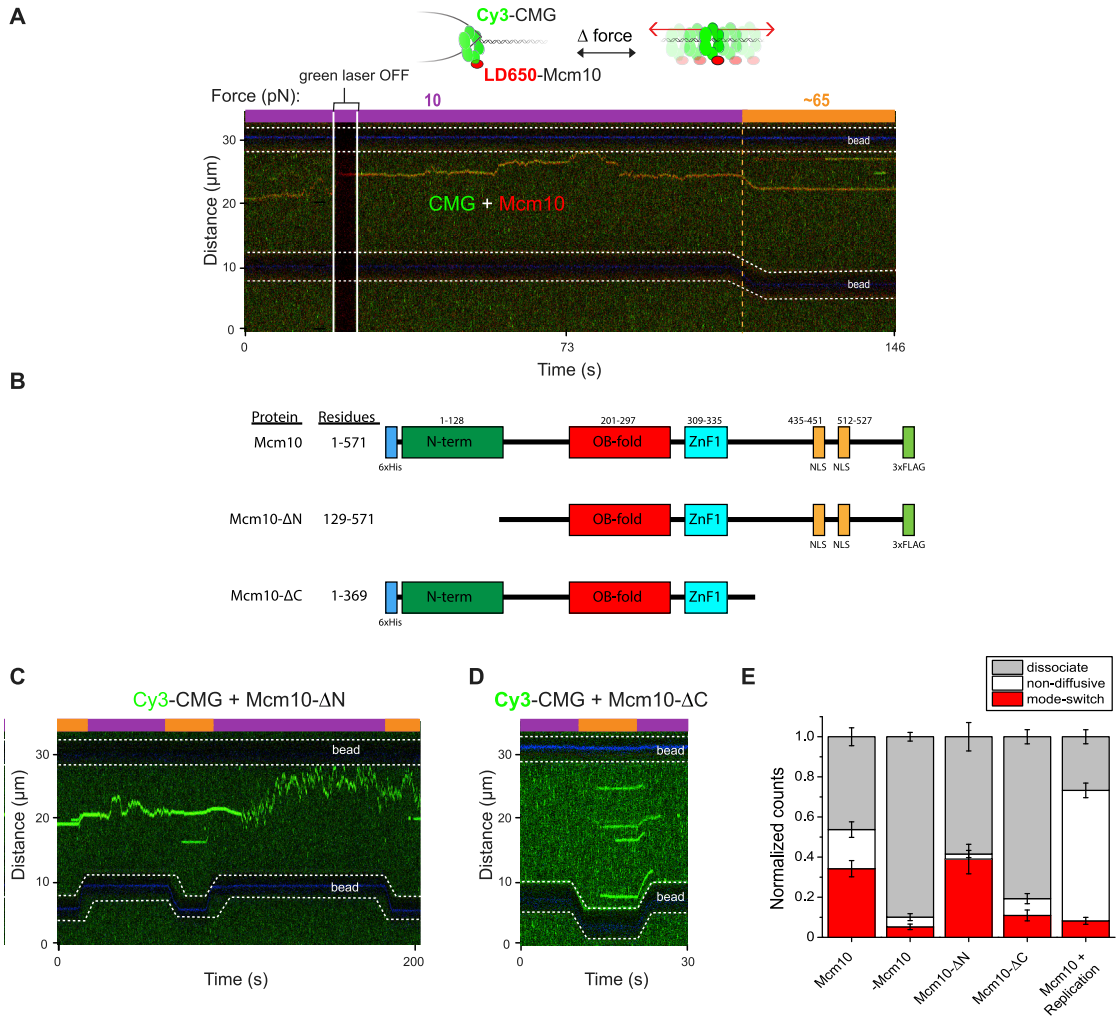

Figure S5. Additional Characterization of CMG Behavior upon Fork Collapse in the Presence of Wild-Type or Mutant Mcm10, Related to Figure 6

(A) Experiments performed with Cy3-CMG (green) and LD650-Mcm10 (red) demonstrating that Mcm10 travels with CMG in the diffusive mode. The green laser was briefly turned off to confirm the red fluorescence signal from Mcm10.

(B) Domain organization of full-length *S. cerevisiae* Mcm10 (top), and truncations tested in this study (middle, bottom). Strains harboring Mcm10-ΔN show no growth defects, whereas Mcm10-ΔC does not support yeast survival (Lõoke et al., 2017). OB-fold: oligonucleotide/oligosaccharide binding fold; ZnF1: zinc-finger motif 1; NLS: nuclear localization sequence.

(C) Representative kymograph demonstrating that Mcm10-ΔN supports CMG mode-switching.

(D) Representative kymograph demonstrating that Mcm10-ΔC rarely supports CMG mode-switching.

(E) Distribution quantitation of the fate of fork-loaded CMG under various conditions. CMG at the fork may follow one of three fates upon lowering of the tension and strand reannealing: 1) mode-switch to fast diffusion on dsDNA; 2) remain at the fork (non-diffusive); or 3) dissociate. Note that in the presence of replication components, the non-diffusive cases display directed motion. Error bars represent SEM.

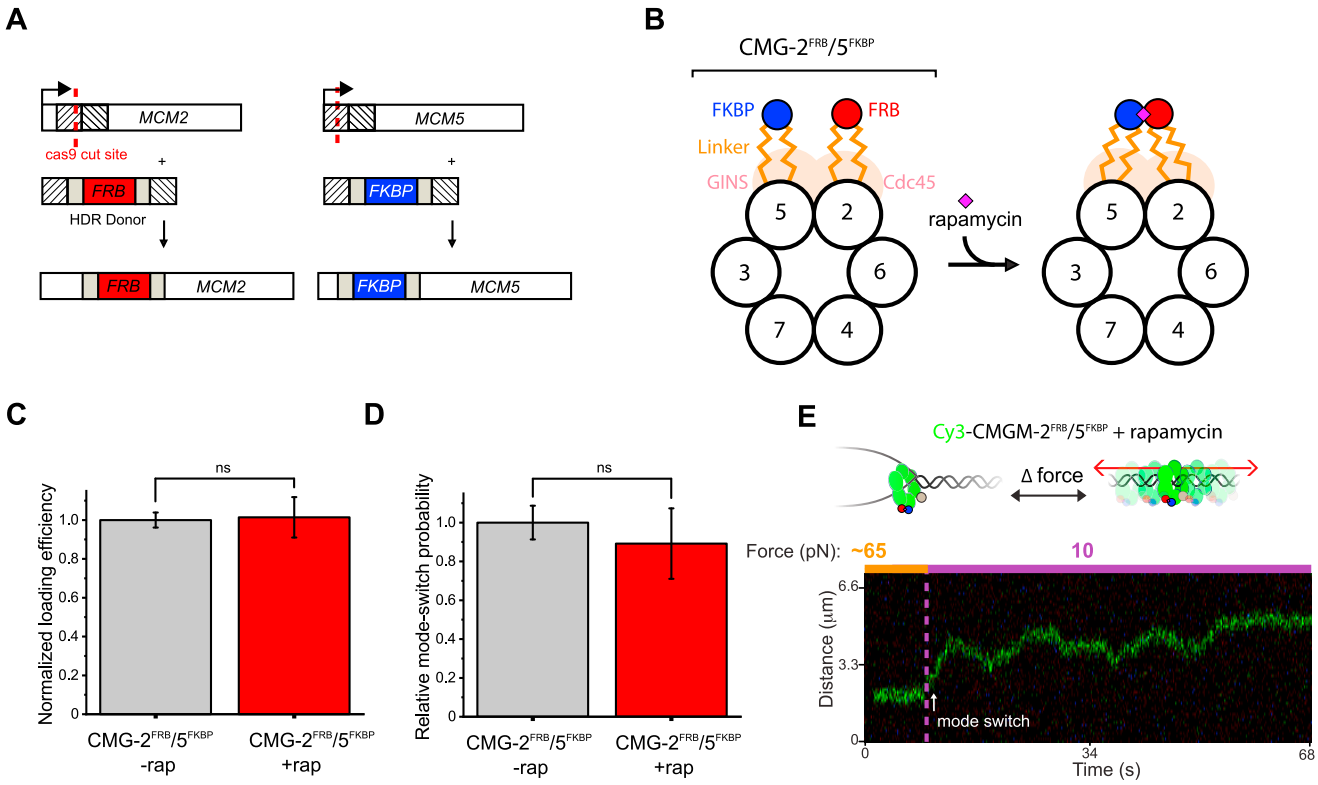

Figure S6. Mcm2/5 Gate Mutant Shows No Deficiency in ssDNA Gating, Related to Figure 6

(A) Schematic of the CRISPR/Cas9 genome editing used to produce CMG with a rapamycin-inducible linkage between Mcm2-FRB and Mcm5-FKBP.

(B) Cartoon illustrating the rapamycin-inducible linkage in CMG engineered in (A).

(C) Normalized loading efficiency of CMG-Mcm2/5 and Mcm10 onto ssDNA in the absence or presence of 1 μM rapamycin ($p = 0.9151$). Following dragging to an orthogonal channel lacking CMG, stable loading was determined by the average fluorescence intensity along the tether during the next 20 frames. Values were normalized to the no-rapamycin case. Error bars represent SEM.

(D) Relative mode-switching probability of CMG-Mcm2/5 plus Mcm10 in the absence or presence of 1 μM rapamycin ($p = 0.6951$). Error bars represent SEM.

(E) Representative kymograph demonstrating that CMG-Mcm2/5 plus Mcm10 mode-switches in the presence of a sealed Mcm2/5 interface.

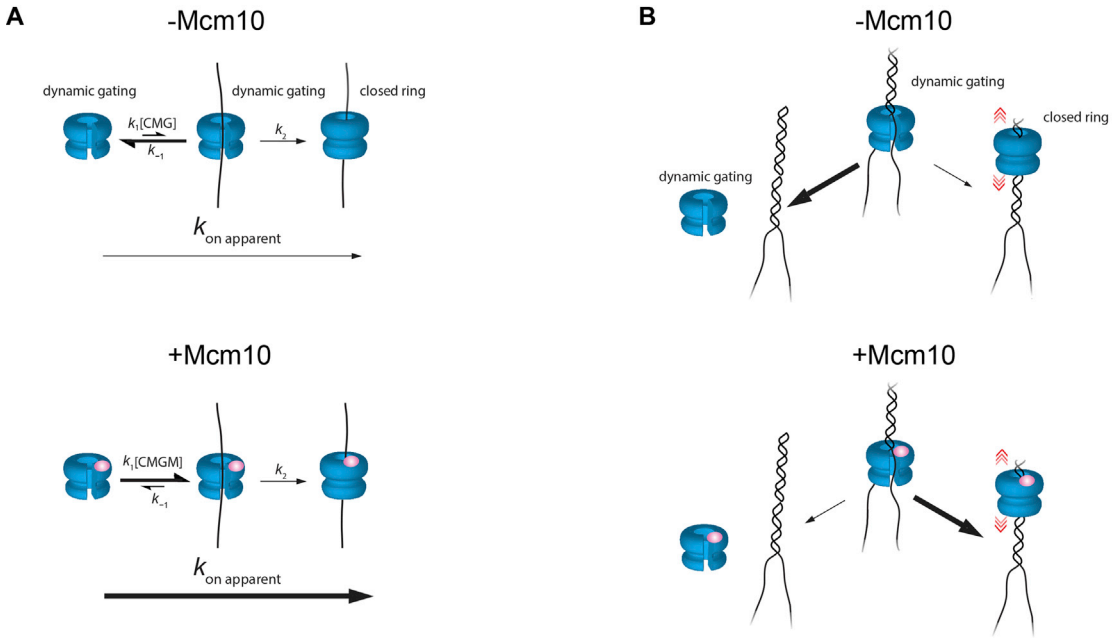

Figure S7. Model for CMG ssDNA Gating and Mcm10 Effect, Related to Figure 7

(A) CMG exhibits transient ssDNA gate opening in solution. In the absence of Mcm10, interaction of CMG with ssDNA is usually too short-lived ($k_{-1} >> k_1$[CMG]) for CMG to open and close its gate around ssDNA (top). Nonetheless, rare but successful encirclement leads to a conformational change in CMG (k_2) in which the gate remains stably closed. Mcm10 greatly increases the affinity of CMG for ssDNA, ensuring sufficient dwell time on ssDNA to allow for encirclement and stable loading (bottom). The aggregate rate constant $k_{\text{on apparent}}$ describes this entire process, and is significantly increased by Mcm10.

(B) When uncoupled from a polymerase, CMG at the fork is prompted by the reannealing strands to switch from a closed-ring conformation to one that is transiently open. In the absence of Mcm10, the transiently open form of CMG interacts too weakly with the duplex to result in dsDNA encirclement, so dissociation is favored (top). Mcm10 greatly enhances the affinity of CMG for DNA, allowing sufficient time for robust dsDNA encirclement and diffusion (bottom).